



Nitrogen isotope evidence for an oligotrophic shallow ocean during the Cambrian Stage 4

Chao Chang^{a,b,*}, Wenxuan Hu^b, Xiaolin Wang^b, Kang-Jun Huang^a, Aihua Yang^b
Xingliang Zhang^a

^a Shaanxi Key Laboratory of Early Life and Environment, State Key Laboratory of Continental Dynamics, and Department of Geology, Northwest University, Xi'an 710069, China

^b State Key Laboratory for Mineral Deposits Research, Institute of Energy Sciences, School of Earth Sciences and Engineering, Nanjing University, Nanjing 210046, China

Received 23 February 2019; accepted in revised form 22 April 2019; available online 8 May 2019

Abstract

Following the Cambrian Explosion, a significant extinction event occurred during the Cambrian Stage 4, with the extinction rate second only to that experienced in the end-Permian. To figure out the variation of N supply and elucidate the combined effect of O₂ and N availability on the extinction event, this study presents the first set of high-resolution N isotope data from two shallow-water Cambrian Stage 4 drilling sections on the eastern Yangtze Platform. The results indicate that the sections are characterized by highly negative $\delta^{15}\text{N}$ signatures during the lowermost and uppermost Cambrian Stage 4, which are indicative of strong NH₄⁺ assimilation in an anoxic shallow ocean. During the rest of the Cambrian Stage 4, both of the study sections show stable $\delta^{15}\text{N}$ values close to 0. This phenomenon can be best explained by enhanced N₂ fixation in an oxic shallow ocean characterized by strong N limitation, resembling the low-latitude oligotrophic regions in the modern ocean. The oligotrophic environment was likely caused by enhanced denitrification/anammox as well as elevated P input associated with eustatic changes, and may have been widespread in the global shallow ocean during the Cambrian Stage 4. Our results lend new support to the traditional view that anoxia contributed to the mass extinction event. More importantly, it is emphasized that the oligotrophic environment may have played an important role in the prolonged decline of metazoan diversity during this stage.

© 2019 Elsevier Ltd. All rights reserved.

Keywords: Nitrogen supply; Oligotrophy; Extinction event; Eustatic changes

1. INTRODUCTION

During the latest Ediacaran to Cambrian Stage 3, Earth's biosphere witnessed an abrupt diversification of bilateral lineages and the sudden appearance of most pre-

sent animal phyla (Knoll and Carroll, 1999; Morris, 2000; Shu et al., 2014; Zhang and Shu, 2014; Zhang et al., 2017). This extraordinary biological evolutionary event is termed the “Cambrian explosion” (Cloud, 1948). Subsequently however, the Cambrian evolutionary fauna experienced a significant extinction event during the Cambrian Stage 4, with the extinction rate second only to that experienced in the end-Permian (Benton, 1995; Li et al., 2007; Zhu et al., 2018).

The extinction event was mainly attributed to anoxic events associated with large-amplitude eustatic changes or

* Corresponding author at: Shaanxi Key Laboratory of Early Life and Environment, State Key Laboratory of Continental Dynamics, and Department of Geology, Northwest University, Xi'an 710069, China.

E-mail address: changchao@nwu.edu.cn (C. Chang).

global volcanic activities in previous studies (Zhuravlev and Wood, 1996; Montañez et al., 2000; Zhu et al., 2004; Hough et al., 2010; Jourdan et al., 2014). However, recent iron speciation and pyrite morphology works indicated that the shallow ocean was dominantly oxic or suboxic during the Cambrian Stage 4 (Faggetter et al., 2017; Li et al., 2017). This excludes anoxia as the sole cause for the prolonged substantial decline of metazoan diversity throughout this stage and calls for further investigations on the impact of other metabolically important environmental factors (Li et al., 2007).

Except for O₂, nutrient and food availability has long been considered as a possible driving force for early animal evolution during the Ediacaran–Cambrian transition (Cook and Shergold, 1984; Brasier, 1992; Cook, 1992). Recent geobiological works lent new support to this view, demonstrating that early animal communities were likely more food limited than generally appreciated (Leys and Kahn, 2018; Sperling and Stockey, 2018). Primary producers provide fundamental food sources for animals, and their productivity is closely associated with nutrient availability in the ocean. Nitrogen, phosphorous, and iron are the major nutrient elements limiting biological productivity in the modern ocean. About 30% of the ocean's surface area is characterized by high-macronutrient, Fe-limited systems, while most of the remaining low-latitude systems are N-limited or in places co-limited by N and P (Moore et al., 2013). In the redox-stratified ocean during the early Cambrian, N limitation could be more common as a result of significant N loss through denitrification or anammox as well as low N:P ratios caused by enhanced P supply to the shallow ocean, aggravating the controlling effect of N availability on biological development (Zhuravlev and Wood, 1996; Ader et al., 2016; Jin et al., 2016; Li et al., 2017).

The N isotopic composition of marine sediments can not only provide clues about ocean redox structure but also reveal the availability of different N species, such as NH₄⁺ and NO₃⁻, in the water column in the geologic history (Sigman et al., 2009; Stüeken et al., 2016). Therefore, nitrogen isotopic signatures hold great potential to provide a more complete understanding of environmental influences on biotic radiation and extinction events during the early Cambrian. In view of this, extensive nitrogen isotopic studies were carried out in recent years and the results indicated that the variation of fixed nitrogen supply was likely a major cause of episodic animal radiations and declines during the Ediacaran–Cambrian transition (Cremonese et al., 2013, 2014; Cai et al., 2015; Wang et al., 2015, 2018a). However, due to a lack of nitrogen isotope data, little remains known about the oceanic nitrogen cycle during the Cambrian Stage 4.

To figure out the variation of N supply and elucidate the combined effect of O₂ and N availability on the extinction event during the Cambrian Stage 4, this work presents the first set of high-resolution N isotope data from two shallow-water Cambrian Stage 4 drilling sections in Well K2 and Well WN2 on the eastern Yangtze Platform. Underground burial has protected the sections from surface weathering and facilitated preservation of primary

geochemical records. The completeness of the sections (Chang et al., 2017) offers an opportunity for tracking the evolution of biogeochemical processes in the shallow ocean throughout the Cambrian Stage 4. The results supplement important information concerning the nitrogen cycle and variation of N availability in the ocean, and provide new insights on the cause of the extinction event during this stage.

2. GEOLOGICAL SETTING

During the early Cambrian, South China was an isolated craton located at middle latitudes of the Northern Hemisphere (Fig. 1A; Li et al., 2008). It comprised the Yangtze and Cathaysia tectonic blocks that were sutured together during the mid-Neoproterozoic (Fig. 1A; Wang and Li, 2003). During the Ediacaran–Cambrian transition, the Yangtze Block gradually evolved from a rift to a passive continental margin basin under extensional tectonic movement (Wang and Li, 2003). A variety of sedimentary successions deposited across the Yangtze Block during the Cambrian Series 2, spanning from shore to basin facies (Yang et al., 2005). The study area in this work was located on the eastern Yangtze Block (Fig. 1A). The paleogeography of this area was characterized by a central–lateral uplifted region with depressions to its north and south (Fig. 1B; Lu and Ji, 2013). Sedimentary successions in this area can be roughly divided into two facies zones: platform to shelf edge facies zone and outer shelf to slope facies zone (Fig. 1B). The platform to shelf edge facies zone is characterized by limestone and dolostone interbedded with mudstone, while the outer shelf to slope facies zone is represented by limestone, carbonaceous mudstone, and siliceous mudstone. The abundance of carbonaceous and siliceous mudstone increases from the outer shelf to slope areas.

Well K2 is located close to Kunshan City, within the platform facies zone during the Cambrian Stage 4 (Fig. 1B). Rock units in the drilling section include the uppermost Dengying, Mufushan, and lowermost Paotaihan formations (Fig. 2A). The Dengying Formation comprises mainly dolostone and interbedded chert, and is unconformably overlain by the Mufushan Formation comprising mainly limestone and argillaceous limestone, with thin (several cm thickness) calcareous–dolomitic mudstone interlayers. The upper part of the Mufushan Formation has a higher dolomite content than the lower part, with a black carbonaceous mudstone unit of ~10 m thickness in its middle part. The Paotaihan Formation conformably overlies the Mufushan Formation and comprises mainly light gray to reddish dolostone. The lower boundary of the formation is the traditional Lower–Middle Cambrian boundary. Paleontological records (Zhang and Zhou, 1985) and inorganic C isotope curves (Chang et al., 2017) indicate that the sedimentary age of the Mufushan Formation spanned from the late Cambrian Stage 3 to latest Cambrian Stage 4.

Well WN2 is located southeast of Xuancheng City, within the outer-shelf facies zone during the Cambrian Stage 4 (Fig. 1B). Rock units in the well section include

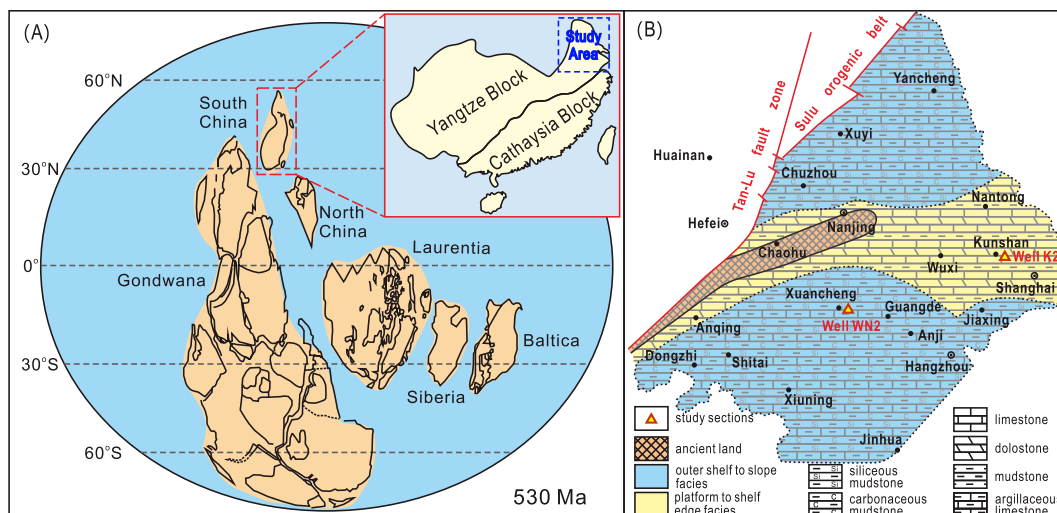


Fig. 1. (A) Early Cambrian global paleogeography (modified from Li et al., 2008). South China consisted of Yangtze and Cathaysia blocks. The study area was on the eastern Yangtze Block. (B) Paleogeography of the eastern Yangtze Block during Cambrian Series 2 (modified from Lu and Ji, 2013).

the uppermost Xijiashan Formation, Hetang, Dachenling, and lowermost Yangliugang formations (Fig. 2B). The Hetang Formation comprises mainly siliceous mudstone with interbedded calcareous mudstone, and is conformably overlain by the Dachenling Formation. The Dachenling Formation is characterized by alternating limestone and mudstone units. The lithologies of these units include limestone, argillaceous limestone, calcareous mudstone, and siliceous mudstone. The Dachenling Formation is conformably overlain by the Yangliugang Formation, which comprises mainly limestone and siliceous mudstone. The lower boundary of the Yangliugang Formation is the traditional Lower–Middle Cambrian boundary (Chu et al., 2016). Paleontological records of adjacent areas (Zhu et al., 2005) and inorganic C isotope plots (Chang et al., 2017) indicate that the sedimentary age of the Dachenling Formation spanned the early–latest Cambrian Stage 4.

3. SAMPLES AND METHODS

Sampling locations are shown on the lithological columns of wells K2 and WN2 in Fig. 2. A total of 79 samples were taken from the Well K2 section, including 7 from the Paotaishan Formation and 72 from the Mufushan Formation (Fig. 2A). The depth of the samples ranges from 280.0 m to 555.7 m. A total of 111 samples were taken from the Well WN2 section, including 26 from the Yangliugang Formation, 41 from the Dachenling Formation, and 44 from the Hetang Formation (Fig. 2B). The depth of the samples ranges from 429.6 m to 625.3 m. Fresh interiors of selected samples were chipped and ground (200 mesh) prior to geochemical analyses.

Nitrogen isotopic analyses were undertaken with a Thermo Finnigan Elemental Delta V Advantage mass spectrometer coupled to a Thermo 1112 Flash Elemental Analyzer via a Thermo ConFloIII Interface, at the Third Institute of Oceanography, State Oceanic Administration,

Xiamen, China. Powdered samples were decalcified overnight in 6 M HCl, and the solutions centrifuged to remove chloride residues. The residue was dried at 60 °C overnight and re-ground. 10–100 mg samples were weighed for N isotopic analyses, and δ values are reported relative to air, with analytical errors better than $\pm 0.3\text{‰}$. Acetanilide 1 (Indiana University: $\delta^{15}\text{N} = +1.18\text{‰}$) was used as the nitrogen stable isotope standards. The results were not blank-corrected because the amount of blank nitrogen was negligible compared to the sample sizes and the blank correction was expected to be within the measurement errors. Total nitrogen (TN) contents were obtained during isotopic measurements from the nitrogen plot area.

Organic C isotopic analyses were undertaken with a Finnigan MAT 253 isotope ratio mass spectrometer at the Experimental Research Center, SINOPEC Petroleum Exploration and Development Research Institution, Wuxi, China. Powdered samples were treated with hot 2 M HCl for 2 h to remove carbonates. Residues were dried at room temperature then heated with CuO in an evacuated quartz glass tube at 650 °C for 5 h to convert organic carbon to CO_2 . The CO_2 was collected and purified on a cryogenic vacuum line. The analytical results are expressed in the standard δ notation with respect to the PDB standard, with a standard deviation of $\pm 0.2\text{‰}$. GB04407 (China national standards: $\delta^{13}\text{C}_{\text{org}} = -22.43\text{‰}$) was used as the carbon stable isotope standards. The results were not blank-corrected because the amount of blank carbon was negligible compared to the sample sizes and the blank correction was expected to be within the measurement errors.

Total organic carbon (TOC) analyses were carried out on a Vario EL3 element analyzer at the Ministry of Education Key Laboratory of Surficial Geochemistry, Department of Earth Sciences, Nanjing University, Nanjing, China. Approximately 2 g of powdered sample was treated with 2 M HCl for 48 h to remove carbonates. The solution was then centrifuged at 4500 rpm for 15 min, after which

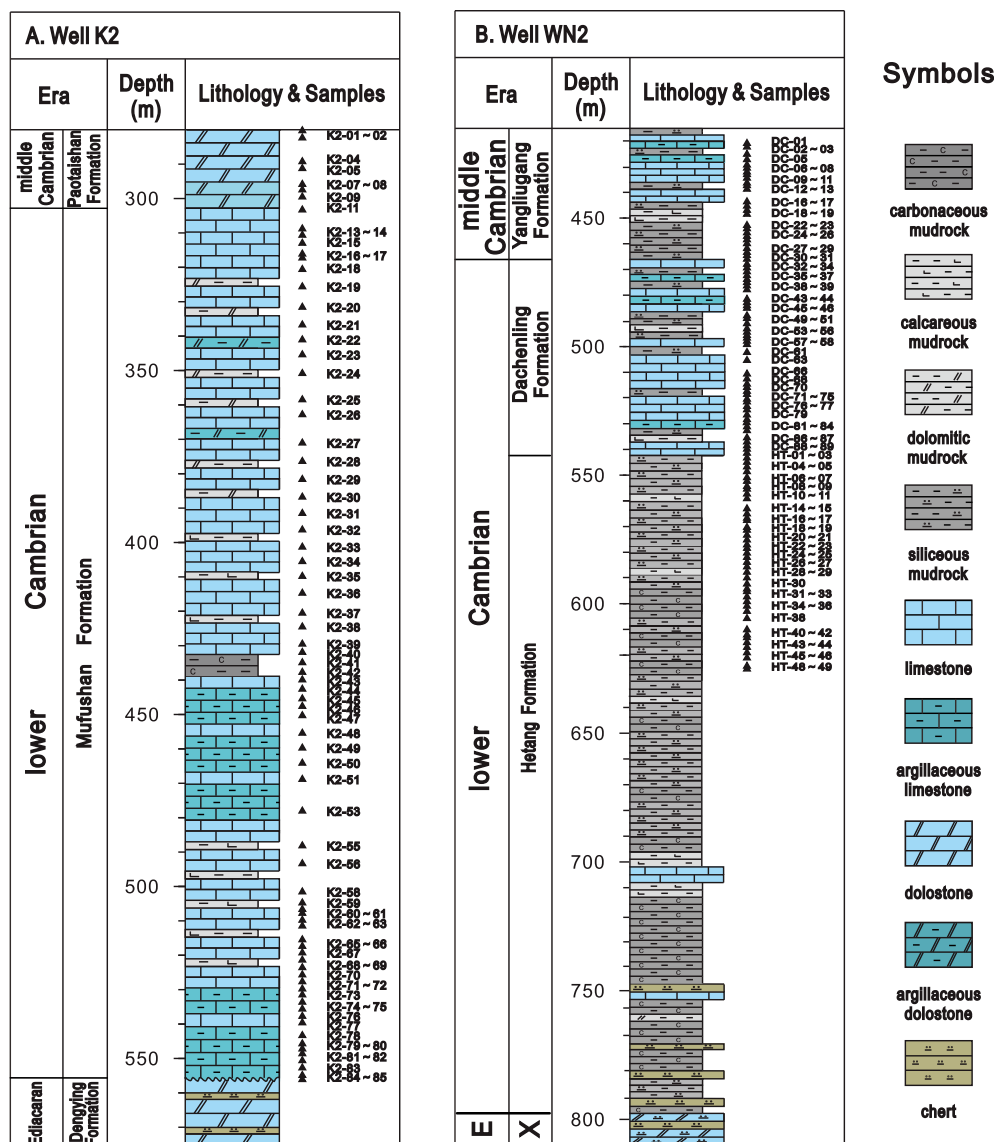


Fig. 2. Lithological columns of the Well K2 section (A) and Well WN2 section (B). E and X in the Era column of (B) represent Ediacaran and Xijianshan Formation, respectively.

the solid residue was mixed with deionized water. Centrifugation was repeated ~ 6 times until the pH of the solution reached ~ 7 . The solid residue was then dried at 60°C for 24 h and re-ground in an agate mortar. Samples of 20–50 mg were used for TOC analyses. Analytical uncertainties were estimated to be less than 5%.

4. RESULTS

TOC and TN contents, atomic C/N ratios, as well as organic C and N isotopic compositions are presented in Tables 1 and 2 and Figs. 3 and 4. TOC data for carbonate samples are from Chang et al. (2017).

4.1. Well K2 section

TOC contents in the section displays an overall decreasing upward trend. Argillaceous limestone units in the lower

and middle parts of the Mufushan Formation have TOC contents as high as 7.3 and 2.6 wt.%, respectively; while in the rest of the section, TOC contents are generally < 1 wt.% (Fig. 3). TN contents of bulk samples in the section vary from 0.003 to 0.111 wt.%, with high TN contents occurring in argillaceous limestone units in the Mufushan Formation (Table 1).

C/N ratios range from 5.4 to 113.4, with an average of 38.5 (Table 1). The ratios decrease from > 100 to < 20 from the lower to middle parts of the Mufushan Formation, and remain constant in the upper part. An increase in ratios occurs at the boundary between the Mufushan and Paotaisihan formations (Fig. 3).

In the lower part of the Mufushan Formation (560–480 m), organic C isotopic compositions display an overall positive excursion, with $\delta^{13}\text{C}_{\text{Org}}$ values increasing from about -34‰ to -26‰ , before decreasing to about -32‰ (Fig. 3). In the rest of the section, $\delta^{13}\text{C}_{\text{Org}}$ values mostly

Table 1
Analytical results of $\delta^{13}\text{C}_{\text{org}}$, $\delta^{15}\text{N}$, TOC and TN of samples from the Well K2 section.

| Samples | Lithology | Depth (m) | TOC (wt. %) | TN (wt. %) | C/N | $\delta^{13}\text{C}_{\text{org}}$ (‰) | $\delta^{15}\text{N}$ (‰) |
|----------------------------|------------------------|-----------|-------------|------------|------|--|---------------------------|
| <i>Paotaihan formation</i> | | | | | | | |
| K2-01 | Dolostone | 280.0 | 0.0 | 0.003 | 15.7 | −28.8 | |
| K2-02 | Dolostone | 282.1 | 0.0 | 0.004 | 10.0 | −30.2 | |
| K2-04 | Dolostone | 289.0 | 0.0 | 0.004 | 8.4 | −29.9 | |
| K2-05 | Dolostone | 290.9 | 0.1 | 0.009 | 7.6 | −30.9 | |
| K2-07 | Dolostone | 294.7 | 0.3 | 0.009 | 33.9 | −30.6 | 3.6 |
| K2-08 | Dolostone | 297.5 | 0.1 | 0.003 | 42.0 | −30.3 | 5.0 |
| K2-09 | Dolostone | 299.1 | 0.4 | 0.006 | 87.5 | −29.6 | 3.2 |
| <i>Mufushan formation</i> | | | | | | | |
| K2-11 | Limestone | 303.8 | 0.4 | 0.008 | 64.8 | −30.0 | 3.6 |
| K2-13 | Limestone | 307.3 | 0.5 | 0.009 | 62.6 | −30.4 | 5.1 |
| K2-14 | Limestone | 310.4 | 0.2 | 0.008 | 28.5 | −30.6 | −5.6 |
| K2-15 | Limestone | 312.3 | 0.6 | 0.020 | 33.6 | −30.4 | −4.8 |
| K2-16 | Limestone | 314.6 | 0.6 | 0.025 | 26.8 | −30.3 | −1.2 |
| K2-17 | Limestone | 315.9 | 1.5 | 0.043 | 40.4 | −30.8 | −3.9 |
| K2-18 | Limestone | 319.1 | 0.3 | 0.009 | 33.9 | −29.6 | −2.7 |
| K2-19 | Limestone | 320.2 | 0.3 | 0.011 | 29.6 | −29.5 | −1.9 |
| K2-20 | Limestone | 323.6 | 0.1 | 0.010 | 16.7 | −29.6 | −2.1 |
| K2-21 | Limestone | 328.6 | 0.2 | 0.013 | 15.1 | −30.2 | −0.7 |
| K2-22 | Limestone | 334.6 | 0.5 | 0.039 | 14.7 | −30.4 | −1.2 |
| K2-23 | Limestone | 339.7 | 0.2 | 0.017 | 12.1 | −30.3 | 2.5 |
| K2-24 | Limestone | 344.0 | 0.1 | 0.014 | 10.8 | −30.0 | 1.6 |
| K2-25 | Limestone | 348.4 | 0.3 | 0.039 | 7.5 | −30.7 | 0.8 |
| K2-26 | Limestone | 353.8 | 0.4 | 0.071 | 5.9 | −31.0 | −0.2 |
| K2-27 | Limestone | 361.5 | 0.2 | 0.033 | 6.6 | −30.9 | −1.5 |
| K2-28 | Limestone | 365.8 | 0.3 | 0.043 | 7.4 | −31.0 | −0.9 |
| K2-29 | Limestone | 374.0 | 0.2 | 0.054 | 5.4 | −32.1 | 0.1 |
| K2-30 | Limestone | 379.4 | 0.2 | 0.038 | 6.7 | −32.0 | 0.5 |
| K2-31 | Limestone | 384.6 | 0.2 | 0.028 | 7.5 | −31.6 | 0.8 |
| K2-32 | Limestone | 389.8 | 0.3 | 0.046 | 7.8 | −32.1 | 1.1 |
| K2-33 | Limestone | 394.5 | 0.3 | 0.035 | 8.5 | −32.4 | 2.9 |
| K2-34 | Limestone | 399.3 | 0.3 | 0.043 | 8.2 | −32.2 | 2.3 |
| K2-35 | Limestone | 404.3 | 0.2 | 0.031 | 9.3 | −33.0 | 0.4 |
| K2-36 | Limestone | 408.5 | 0.3 | 0.047 | 7.2 | −33.8 | 1.1 |
| K2-37 | Limestone | 412.8 | 0.5 | 0.085 | 6.4 | −33.5 | 1.3 |
| K2-38 | Limestone | 417.7 | 0.4 | 0.060 | 7.2 | −32.8 | 6.0 |
| K2-39 | Limestone | 423.5 | 0.5 | 0.072 | 7.4 | −31.8 | 3.3 |
| K2-40 | Limestone | 427.5 | 0.5 | 0.073 | 8.5 | −31.6 | 0.1 |
| K2-41 | Limestone | 432.5 | 0.6 | 0.101 | 6.8 | −31.3 | −1.7 |
| K2-42 | Calcareous mudstone | 436.9 | 0.9 | 0.104 | 10.6 | −31.2 | −3.0 |
| K2-43 | Argillaceous limestone | 439.3 | 1.2 | 0.088 | 15.3 | −31.6 | −3.6 |
| K2-44 | Argillaceous limestone | 442.3 | 1.5 | 0.088 | 19.6 | −31.7 | −4.4 |
| K2-45 | Argillaceous limestone | 445.1 | 1.8 | 0.076 | 28.3 | −30.8 | 0.5 |
| K2-46 | Argillaceous limestone | 447.3 | 1.6 | 0.078 | 24.0 | −30.7 | −0.4 |
| K2-47 | Argillaceous limestone | 450.0 | 2.3 | 0.111 | 24.1 | −30.8 | 0.1 |
| K2-48 | Argillaceous limestone | 455.1 | 2.4 | 0.080 | 34.7 | −29.7 | 0.3 |
| K2-49 | Limestone | 459.4 | 0.4 | 0.017 | 25.4 | −30.2 | −0.5 |
| K2-50 | Argillaceous limestone | 463.8 | 1.9 | 0.081 | 26.8 | −30.9 | 0.4 |
| K2-51 | Limestone | 468.5 | 0.7 | 0.098 | 8.0 | −31.8 | −0.5 |
| K2-53 | Argillaceous limestone | 477.7 | 1.9 | 0.067 | 33.6 | −32.1 | −2.2 |
| K2-54 | Argillaceous limestone | 483.6 | 2.6 | 0.089 | 34.3 | −36.2 | −1.2 |
| K2-55 | Limestone | 487.8 | 0.4 | 0.008 | 53.4 | −29.5 | 3.0 |
| K2-56 | Limestone | 493.0 | 0.1 | 0.002 | 48.4 | −29.7 | −0.7 |
| K2-57 | Calcareous mudstone | 497.1 | 1.3 | 0.033 | 44.7 | −33.8 | −2.7 |
| K2-58 | Limestone | 501.2 | 0.2 | 0.004 | 61.1 | −30.0 | 1.4 |
| K2-59 | Limestone | 504.4 | 0.3 | 0.007 | 42.5 | −30.5 | −1.5 |
| K2-60 | Limestone | 506.3 | 0.3 | 0.006 | 53.1 | −30.7 | −2.3 |
| K2-61 | Limestone | 507.4 | 0.5 | 0.010 | 58.9 | −30.6 | −0.2 |
| K2-62 | Limestone | 509.4 | 0.4 | 0.010 | 48.9 | −28.2 | −0.8 |
| K2-63 | Limestone | 511.1 | 1.0 | 0.019 | 62.1 | −28.0 | −1.9 |
| K2-65 | Limestone | 515.1 | 0.5 | 0.007 | 79.3 | −27.5 | −5.4 |

(continued on next page)

Table 1 (continued)

| Samples | Lithology | Depth (m) | TOC (wt. %) | TN (wt. %) | C/N | $\delta^{13}\text{C}_{\text{org}}$ (‰) | $\delta^{15}\text{N}$ (‰) |
|---------|------------------------|-----------|-------------|------------|-------|--|---------------------------|
| K2-66 | Calcareous mudstone | 517.0 | 2.7 | 0.038 | 82.1 | −26.4 | −4.1 |
| K2-67 | Limestone | 518.9 | 0.3 | 0.006 | 57.1 | −28.3 | −2.9 |
| K2-68 | Limestone | 521.0 | 0.3 | 0.004 | 82.0 | −25.9 | −4.7 |
| K2-69 | Calcareous mudstone | 523.2 | 1.7 | 0.030 | 64.4 | −29.2 | −2.0 |
| K2-70 | Limestone | 525.3 | 1.0 | 0.024 | 46.8 | −27.0 | −2.9 |
| K2-71 | Limestone | 527.3 | 1.5 | 0.026 | 64.8 | −29.0 | −1.5 |
| K2-72 | Limestone | 529.4 | 1.0 | 0.025 | 48.3 | −29.4 | −0.4 |
| K2-73 | Argillaceous limestone | 531.1 | 2.1 | 0.055 | 45.1 | −29.1 | −1.8 |
| K2-74 | Argillaceous limestone | 533.2 | 3.6 | 0.058 | 73.4 | −30.2 | −1.6 |
| K2-75 | Argillaceous limestone | 535.2 | 7.0 | 0.096 | 85.5 | −32.9 | −1.9 |
| K2-76 | Argillaceous limestone | 537.3 | 3.5 | 0.039 | 105.0 | −28.4 | −2.7 |
| K2-77 | Limestone | 539.2 | 0.5 | 0.010 | 63.8 | −29.2 | −2.0 |
| K2-78 | Argillaceous limestone | 542.9 | 4.5 | 0.062 | 84.6 | −32.8 | −1.3 |
| K2-79 | Argillaceous limestone | 545.3 | 4.4 | 0.059 | 86.8 | −32.4 | −0.3 |
| K2-80 | Argillaceous limestone | 546.8 | 5.1 | 0.089 | 67.4 | −30.5 | −2.0 |
| K2-81 | Argillaceous limestone | 548.2 | 7.3 | 0.075 | 113.4 | −28.8 | −1.1 |
| K2-82 | Argillaceous limestone | 550.2 | 3.9 | 0.050 | 90.4 | −30.3 | −3.0 |
| K2-83 | Limestone | 552.3 | 0.9 | 0.013 | 81.9 | −30.2 | −0.3 |
| K2-84 | Argillaceous limestone | 554.5 | 2.5 | 0.042 | 68.1 | −30.0 | 0.0 |
| K2-85 | Argillaceous limestone | 555.7 | 2.1 | 0.034 | 72.8 | −29.6 | 0.3 |

fluctuate between -32‰ and -30‰ , except for a negative excursion around 410 m with the lowest $\delta^{13}\text{C}_{\text{org}}$ value of -33.8‰ (Fig. 3; Table 1).

The N isotopic compositions display a negative excursion in the lower part of the Mufushan Formation, overlapping with the depth range of the negative $\delta^{13}\text{C}_{\text{org}}$ excursion (Fig. 3). $\delta^{15}\text{N}$ values decrease from near 0‰ to -6‰ , before increasing to about $+3\text{‰}$. Two additional negative $\delta^{15}\text{N}$ excursions occur in the middle (440–480 m) and at the top (340–310 m) of the Mufushan Formation, with $\delta^{15}\text{N}$ values as low as -6‰ (Fig. 3). In the rest of the formation, $\delta^{15}\text{N}$ values mostly fluctuate between -2‰ and $+1\text{‰}$. In contrast, the Paotaishan Formation has stable positive $\delta^{15}\text{N}$ values of $>+3\text{‰}$.

4.2. Well WN2 section

TOC and TN contents in the section range from 0.1 to 7.5 wt.% and 0.002 to 0.15 wt.%, respectively. Values generally vary with lithology, with values high in mudstone and low in limestone. C/N atomic ratios range from 8.7 to 112.1, with an average of 50.6 (Table 1). Low C/N ratios are associated with high TN contents in the upper Hetang and lower Yangliugang formations (Fig. 4).

In the upper Hetang Formation (630–540 m), $\delta^{13}\text{C}_{\text{org}}$ values increase upwards from -30‰ to -28‰ (Fig. 4). The Dachening Formation is characterized by several negative $\delta^{13}\text{C}_{\text{org}}$ excursions in the mudstone units. $\delta^{13}\text{C}_{\text{org}}$ values remain stable at -28‰ to -27‰ in the limestone units. In the Yangliugang Formation, $\delta^{13}\text{C}_{\text{org}}$ values fluctuate slightly around -30‰ in the mudstone unit, and increase to about -29‰ in the overlying limestone unit (Fig. 4).

The $\delta^{15}\text{N}$ plot shows several positive excursions in the upper Hetang Formation, with values rising to $>+2\text{‰}$ (Fig. 4). In the rest of the formation, values vary mostly between -1‰ and 0‰ , except for an abrupt negative excursion at 580.1–562.9 m. The bottom and top of the Dachening Formation are characterized by strong negative N

isotopic excursions, with $\delta^{15}\text{N}$ values decreasing to $<-3\text{‰}$. In the rest of the Dachening and Yangliugang formations, $\delta^{15}\text{N}$ values mostly fluctuate between -2‰ and $+1\text{‰}$ (Fig. 4).

5. DISCUSSION

5.1. Preservation of primary isotopic signatures

Breakdown and volatilization of organic molecules during diagenetic and metamorphic processes can lead to enrichment of ^{13}C in the remaining organic matter and significant alteration of primary $\delta^{13}\text{C}_{\text{org}}$ signatures can produce a linear $\delta^{13}\text{C}_{\text{org}}$ –TOC in sedimentary rocks (Hayes et al., 1983). The lack of evident correlations between $\delta^{13}\text{C}_{\text{org}}$ and TOC in the sections indicates that carbon isotope signatures of the study sections may have not been significantly altered during diagenetic processes (Figs. 5A and 6A; e.g., Bekker et al., 2008; Ader et al., 2009). An overall covariation of $\delta^{13}\text{C}_{\text{org}}$ and $\delta^{13}\text{C}_{\text{carb}}$ values (Fig. 7) as well as $\delta^{13}\text{C}_{\text{org}}$ data (-34‰ to -26‰) comparable to the Cambrian sedimentary successions reported in previous studies also lend support to limited late-stage alteration of carbon isotope signatures in the study sections (Bekker et al., 2008; Jiang et al., 2012; Cremonese et al., 2013; Guo et al., 2013).

Nitrogen in sedimentary rocks generally occurs in two forms, as organic-bound nitrogen with broadly uniform C/N ratios, or inorganic clay-bound nitrogen devoid of carbon (Ader et al., 2016; Stüeken et al., 2016). Both of the study sections are characterized by strong linear TN–TOC correlations, reflecting a major nitrogen source from primary organic matter (Figs. 5B and 6B; Calvert, 2004). Notably, the upper part (320–435 m) of the Mufushan Formation in Well K2 section shows distinctively high TN contents versus TOC contents (Fig. 5B). Metasomatic addition of N through NH_4^+ -enriched fluids during diagenesis could result in enrichment of N in sedimentary rocks (e.g., Bebout, 1997; Schimmelmann et al., 2009; Stüeken et al.,

Table 2
Analytical results of $\delta^{13}\text{C}_{\text{org}}$, $\delta^{15}\text{N}$, TOC and TN of samples from the Well WN2 section.

| Samples | Lithology | Depth (m) | TOC (wt. %) | TN (wt. %) | C/N | $\delta^{15}\text{N}$ (‰) | $\delta^{13}\text{C}_{\text{org}}$ (‰) |
|------------------------------|------------------------|-----------|-------------|------------|-------|---------------------------|--|
| <i>Yangliugang formation</i> | | | | | | | |
| DC-01 | Argillaceous limestone | 420.6 | 3.3 | 0.060 | 65.0 | −0.1 | −29.4 |
| DC-02 | Limestone | 422.0 | 0.9 | 0.015 | 72.4 | 0.1 | −29.4 |
| DC-03 | Argillaceous limestone | 424.8 | 3.2 | 0.079 | 46.5 | −1.0 | −29.4 |
| DC-05 | Argillaceous limestone | 426.9 | 2.2 | 0.028 | 89.8 | −1.1 | −29.0 |
| DC-06 | Limestone | 428.7 | 0.1 | 0.002 | 35.4 | −0.5 | −28.3 |
| DC-07 | Limestone | 430.2 | 0.8 | 0.012 | 74.3 | −0.1 | −29.1 |
| DC-08 | Limestone | 431.7 | 0.4 | 0.008 | 57.4 | 0.2 | −28.4 |
| DC-09 | Limestone | 432.7 | 2.3 | 0.056 | 47.1 | −0.1 | −28.4 |
| DC-10 | Limestone | 434.1 | 0.5 | 0.008 | 69.0 | 0.1 | −28.9 |
| DC-11 | Calcareous mudstone | 436.0 | 4.5 | 0.147 | 36.1 | 0.9 | −29.0 |
| DC-12 | Limestone | 437.0 | 1.7 | 0.030 | 65.5 | 1.7 | −29.4 |
| DC-13 | Limestone | 438.4 | 1.6 | 0.030 | 60.8 | 1.1 | −29.4 |
| DC-16 | Limestone | 443.3 | 1.3 | 0.040 | 39.6 | 0.1 | −28.9 |
| DC-17 | Siliceous mudstone | 444.1 | 3.3 | 0.088 | 43.5 | −0.2 | −29.8 |
| DC-18 | Calcareous mudstone | 446.6 | 4.4 | 0.090 | 56.8 | −0.6 | −29.6 |
| DC-19 | Calcareous mudstone | 448.0 | 3.2 | 0.077 | 49.3 | 2.0 | −29.8 |
| DC-22 | Calcareous mudstone | 452.5 | 3.2 | 0.093 | 40.7 | 0.0 | −29.8 |
| DC-23 | Siliceous mudstone | 454.0 | 3.3 | 0.128 | 29.6 | −0.8 | −29.8 |
| DC-24 | Siliceous mudstone | 455.4 | 4.0 | 0.146 | 31.8 | 1.2 | −29.8 |
| DC-25 | Siliceous mudstone | 457.0 | 2.5 | 0.122 | 24.0 | 1.0 | −29.8 |
| DC-26 | Siliceous mudstone | 458.4 | 2.1 | 0.120 | 20.6 | 0.4 | −29.7 |
| DC-27 | Siliceous mudstone | 459.8 | 2.9 | 0.126 | 26.8 | 3.5 | −29.8 |
| DC-28 | Siliceous mudstone | 461.3 | 3.4 | 0.107 | 37.2 | 1.0 | −29.8 |
| DC-29 | Siliceous mudstone | 462.8 | 3.9 | 0.138 | 33.2 | −2.1 | −29.8 |
| DC-30 | Siliceous mudstone | 464.2 | 3.4 | 0.132 | 30.5 | 0.5 | −30.0 |
| DC-31 | Siliceous mudstone | 465.8 | 2.5 | 0.116 | 25.2 | −0.2 | −30.0 |
| <i>Dachenling formation</i> | | | | | | | |
| DC-32 | Calcareous mudstone | 467.6 | 4.5 | 0.127 | 41.5 | −2.5 | −30.1 |
| DC-33 | Limestone | 469.0 | 0.5 | 0.011 | 58.3 | −1.6 | −30.2 |
| DC-34 | Argillaceous limestone | 470.5 | 2.7 | 0.045 | 70.3 | −2.8 | −29.7 |
| DC-35 | Argillaceous limestone | 472.0 | 2.9 | 0.045 | 74.6 | −2.8 | −29.8 |
| DC-36 | Limestone | 473.5 | 0.5 | 0.015 | 38.9 | −0.3 | −28.8 |
| DC-37 | Limestone | 474.7 | 0.6 | 0.006 | 108.6 | 1.4 | −28.5 |
| DC-38 | Limestone | 476.0 | 1.0 | 0.011 | 112.1 | 0.4 | −28.4 |
| DC-39 | Limestone | 477.5 | 0.8 | 0.025 | 38.3 | 3.4 | −27.9 |
| DC-43 | Limestone | 481.2 | 0.9 | 0.033 | 31.9 | −0.2 | −27.3 |
| DC-44 | Argillaceous limestone | 482.5 | 3.4 | 0.058 | 68.6 | 0.7 | −26.9 |
| DC-45 | Limestone | 483.7 | 0.4 | 0.013 | 31.8 | −0.3 | −28.4 |
| DC-46 | Limestone | 484.7 | 0.5 | 0.016 | 36.9 | 0.0 | −29.2 |
| DC-49 | Calcareous mudstone | 487.7 | 3.1 | 0.092 | 39.6 | −0.7 | −29.7 |
| DC-50 | Siliceous mudstone | 489.2 | 3.0 | 0.080 | 44.1 | 0.6 | −29.7 |
| DC-51 | Calcareous mudstone | 490.7 | 0.9 | 0.024 | 41.9 | 0.7 | −29.7 |
| DC-53 | Calcareous mudstone | 492.7 | 2.3 | 0.053 | 50.1 | 2.9 | −29.5 |
| DC-54 | Calcareous mudstone | 494.0 | 1.7 | 0.043 | 46.4 | −0.1 | −29.5 |
| DC-55 | Calcareous mudstone | 495.3 | 2.4 | 0.047 | 59.4 | 0.7 | −29.3 |
| DC-56 | Calcareous mudstone | 496.3 | 3.6 | 0.069 | 60.0 | −0.2 | −29.4 |
| DC-57 | Calcareous mudstone | 497.5 | 3.1 | 0.064 | 55.3 | −0.3 | −29.2 |
| DC-58 | Limestone | 498.8 | 0.5 | 0.016 | 32.7 | −0.3 | −27.9 |
| DC-61 | Siliceous mudstone | 502.5 | 5.6 | 0.109 | 59.4 | −0.3 | −28.0 |
| DC-63 | Limestone | 505.0 | 0.2 | 0.011 | 26.0 | 0.2 | −26.9 |
| DC-68 | Limestone | 512.2 | 0.5 | 0.012 | 47.6 | −1.5 | −27.4 |
| DC-70 | Limestone | 514.2 | 0.4 | 0.009 | 46.1 | −1.9 | −28.3 |
| DC-71 | Limestone | 515.5 | 0.4 | 0.012 | 38.2 | −0.1 | −28.1 |
| DC-72 | Limestone | 517.0 | 0.9 | 0.028 | 38.4 | 3.1 | −28.3 |
| DC-73 | Siliceous mudstone | 518.5 | 4.6 | 0.121 | 44.5 | 1.4 | −29.2 |
| DC-74 | Siliceous mudstone | 520.0 | 3.7 | 0.090 | 47.6 | 0.8 | −29.5 |
| DC-75 | Limestone | 521.4 | 0.5 | 0.011 | 53.2 | 0.1 | −27.7 |
| DC-76 | Limestone | 522.9 | 0.5 | 0.012 | 51.4 | −1.9 | −27.2 |
| DC-77 | Limestone | 524.2 | 0.6 | 0.017 | 41.1 | −1.0 | −26.7 |
| DC-79 | Limestone | 526.2 | 0.3 | 0.008 | 46.9 | −1.3 | −26.9 |

(continued on next page)

Table 2 (continued)

| Samples | Lithology | Depth (m) | TOC (wt. %) | TN (wt. %) | C/N | $\delta^{15}\text{N}$ (‰) | $\delta^{13}\text{C}_{\text{org}}$ (‰) |
|-------------------------|------------------------|-----------|-------------|------------|-------|---------------------------|--|
| DC-81 | Limestone | 528.0 | 0.8 | 0.014 | 62.2 | −0.8 | −28.7 |
| DC-82 | Limestone | 529.4 | 0.3 | 0.006 | 65.6 | −3.1 | −31.0 |
| DC-83 | Argillaceous limestone | 530.8 | 2.9 | 0.041 | 81.5 | −2.9 | −31.0 |
| DC-84 | Argillaceous limestone | 532.3 | 3.2 | 0.054 | 68.4 | −3.2 | −30.5 |
| DC-86 | Calcareous mudstone | 535.1 | 3.8 | 0.074 | 60.5 | −4.9 | −30.9 |
| DC-87 | Calcareous mudstone | 536.7 | 3.6 | 0.062 | 67.3 | −3.0 | −30.7 |
| DC-88 | Limestone | 538.2 | 0.4 | 0.006 | 84.2 | −0.9 | −28.7 |
| DC-89 | Limestone | 539.5 | 1.0 | 0.011 | 105.3 | −0.7 | −28.8 |
| <i>Hetang formation</i> | | | | | | | |
| HT-001 | Siliceous mudstone | 541.0 | 7.5 | 0.131 | 66.7 | −0.5 | −28.0 |
| HT-002 | Siliceous mudstone | 543.1 | 5.5 | 0.089 | 71.9 | 2.8 | −28.4 |
| HT-003 | Siliceous mudstone | 545.0 | 4.7 | 0.075 | 72.9 | 4.2 | −28.4 |
| HT-004 | Siliceous mudstone | 546.9 | 4.7 | 0.081 | 67.3 | −0.9 | −28.7 |
| HT-005 | Siliceous mudstone | 548.9 | 4.1 | 0.061 | 78.3 | −1.0 | −28.6 |
| HT-006 | Siliceous mudstone | 550.4 | 3.2 | 0.084 | 44.3 | 0.6 | −29.0 |
| HT-007 | Siliceous mudstone | 551.9 | 3.2 | 0.069 | 53.4 | 1.3 | −29.2 |
| HT-008 | Siliceous mudstone | 553.9 | 3.1 | 0.084 | 43.5 | 0.7 | −29.1 |
| HT-009 | Siliceous mudstone | 554.8 | 3.5 | 0.082 | 49.4 | 1.3 | −29.2 |
| HT-010 | Siliceous mudstone | 556.8 | 3.5 | 0.065 | 63.7 | 2.4 | −28.9 |
| HT-011 | Siliceous mudstone | 558.8 | 3.6 | 0.062 | 67.5 | 1.7 | −29.1 |
| HT-014 | Siliceous mudstone | 562.9 | 2.2 | 0.108 | 23.9 | −1.5 | −29.2 |
| HT-015 | Siliceous mudstone | 564.8 | 1.7 | 0.129 | 15.5 | −1.6 | −28.9 |
| HT-016 | Siliceous mudstone | 566.7 | 1.0 | 0.118 | 9.7 | −1.3 | −28.7 |
| HT-017 | Siliceous mudstone | 568.3 | 1.5 | 0.123 | 14.4 | −1.3 | −28.9 |
| HT-018 | Siliceous mudstone | 569.8 | 1.3 | 0.127 | 11.6 | −1.2 | −29.2 |
| HT-019 | Siliceous mudstone | 570.8 | 0.9 | 0.114 | 8.7 | −0.6 | −28.7 |
| HT-020 | Siliceous mudstone | 572.8 | 1.8 | 0.119 | 18.1 | −1.1 | −29.0 |
| HT-021 | Siliceous mudstone | 574.7 | 2.4 | 0.119 | 23.5 | −1.6 | −28.9 |
| HT-022 | Siliceous mudstone | 576.7 | 2.0 | 0.099 | 23.3 | −1.6 | −29.0 |
| HT-023 | Siliceous mudstone | 578.4 | 2.4 | 0.102 | 27.0 | −2.2 | −29.1 |
| HT-024 | Siliceous mudstone | 580.1 | 2.7 | 0.106 | 30.1 | −1.7 | −29.2 |
| HT-025 | Siliceous mudstone | 582.2 | 3.2 | 0.102 | 36.3 | 3.1 | −29.3 |
| HT-026 | Siliceous mudstone | 584.2 | 2.8 | 0.114 | 28.8 | 1.8 | −29.2 |
| HT-027 | Siliceous mudstone | 586.0 | 3.9 | 0.109 | 42.1 | 2.3 | −29.3 |
| HT-028 | Siliceous mudstone | 587.8 | 4.0 | 0.091 | 50.9 | 0.0 | −29.5 |
| HT-029 | Siliceous mudstone | 589.8 | 3.6 | 0.088 | 47.2 | 2.9 | −29.3 |
| HT-030 | Siliceous mudstone | 591.7 | 3.3 | 0.073 | 52.6 | 1.3 | −29.7 |
| HT-031 | Siliceous mudstone | 593.8 | 4.8 | 0.085 | 65.7 | −0.5 | −29.6 |
| HT-032 | Siliceous mudstone | 595.2 | 3.6 | 0.075 | 56.0 | −0.4 | −29.5 |
| HT-033 | Siliceous mudstone | 596.8 | 2.7 | 0.092 | 34.8 | −0.8 | −29.4 |
| HT-034 | Siliceous mudstone | 598.7 | 4.2 | 0.082 | 60.0 | −0.1 | −29.5 |
| HT-035 | Siliceous mudstone | 600.5 | 3.6 | 0.074 | 57.4 | −0.9 | −29.6 |
| HT-036 | Siliceous mudstone | 602.7 | 5.6 | 0.083 | 79.6 | −0.5 | −29.8 |
| HT-038 | Siliceous mudstone | 606.4 | 5.8 | 0.088 | 77.5 | −0.3 | −29.8 |
| HT-040 | Siliceous mudstone | 610.0 | 5.5 | 0.093 | 68.7 | 1.2 | −29.9 |
| HT-041 | Siliceous mudstone | 611.9 | 3.1 | 0.056 | 65.2 | 0.7 | −29.9 |
| HT-042 | Siliceous mudstone | 613.4 | 4.0 | 0.073 | 64.0 | −0.1 | −30.0 |
| HT-043 | Siliceous mudstone | 615.1 | 5.3 | 0.082 | 75.8 | 0.4 | −30.2 |
| HT-044 | Siliceous mudstone | 617.0 | 3.3 | 0.078 | 49.7 | 1.6 | −29.9 |
| HT-045 | Siliceous mudstone | 618.7 | 3.3 | 0.072 | 53.5 | 2.4 | −30.0 |
| HT-046 | Siliceous mudstone | 620.5 | 4.9 | 0.085 | 67.3 | 1.1 | −30.2 |
| HT-048 | Siliceous mudstone | 624.2 | 4.9 | 0.102 | 55.7 | 1.9 | −30.1 |
| HT-049 | Siliceous mudstone | 625.3 | 5.1 | 0.107 | 55.2 | −1.0 | −30.1 |

2017). However, the Mufushan Formation is overall lack of veins, implying limited impact of late-stage fluid activities and metasomatic alteration (Chang et al., 2017). Alternatively, different correlation gradients for the upper part and the rest of the Mufushan Formation were likely associated with different primary producers or sedimentary environments (Cremonese et al., 2013). In comparison, the deviating data points are distributed roughly in parallel to

the linearly correlated data points (circled by dotted lines) in the TN-TOC cross plot of Well WN2 section (Fig. 6B). Comparatively high TN contents in the samples can be attributed to higher contents of inorganic N bound in clay minerals (Cremonese et al., 2013; Kikumoto et al., 2014; Wang et al., 2015). The deviating data points in the TN-TOC cross plots of Well WN2 section which appear to have much higher nitrogen contents than expected from their

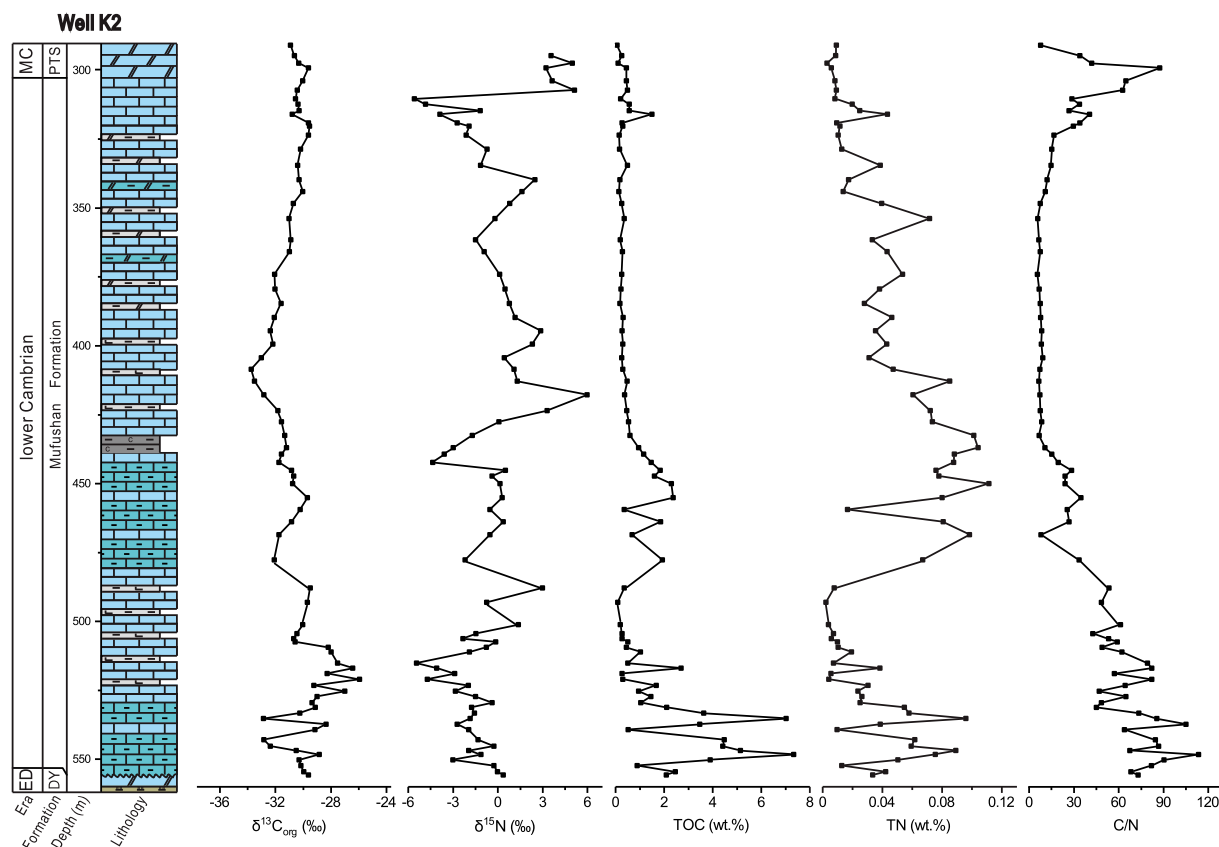


Fig. 3. Chemostratigraphic column of the Well K2 section. ED, DY, MC, and PTC represent Ediacaran, Dengying Formation, middle Cambrian, and Paotaishan Formation, respectively.

TOC values. The lack of strong correlations between TOC contents and C/N ratios in the sections indicates limited loss of organic nitrogen during diagenesis and metamorphism (Figs. 5C and 6C; Cremonese et al., 2013; Kikumoto et al., 2014; Wang et al., 2015; Wang et al., 2018b).

The potential for diagenetic and metamorphic alteration is a major challenge in nitrogen isotope studies of ancient rocks (reviewed by Robinson et al., 2012; Ader et al., 2016; Stüeken et al., 2016). Diagenetic effects on nitrogen isotope differ markedly between anoxic and oxic depositional environments. Under oxic conditions, $\delta^{15}\text{N}$ values of bulk sediments can increase by up to $\sim 4\text{‰}$ as a result of isotopic fractionations during NH_4^+ release and partial oxidation in pore waters (Altabet et al., 1999; Freudenthal et al., 2001; Lehmann et al., 2002; Prokopenko et al., 2006; Möbius, 2013). Positive $\delta^{15}\text{N}$ values $> +2\text{‰}$ in sedimentary rocks may more or less have been altered and elevated during oxic diagenesis (Stüeken et al., 2017). However, most samples in the study sections show $\delta^{15}\text{N}$ values $< +2\text{‰}$, reflecting overall limited alteration of primary $\delta^{15}\text{N}$ signatures through oxic diagenesis. Under anoxic conditions, more than half of the organic nitrogen can be converted to clay-bound NH_4^+ , with small isotopic fractionations of $< 1\text{‰}$ (Müller, 1977; Altabet et al., 1999; Lehmann et al., 2002; Thunell et al., 2004).

In addition, preferential volatilization of isotopically light NH_3 or N_2 during metamorphism can result in ele-

vated $\delta^{15}\text{N}$ values of bulk sediments (Ader et al., 2014). The degree of $\delta^{15}\text{N}$ alteration is closely related to the metamorphic grade of sedimentary rocks, normally $< 1\text{‰}$ below greenschist facies, within 1–2‰ for greenschist facies, within 3–4‰ for amphibolite facies, and up to 6–10‰ for upper amphibolite conditions (reviewed by Ader et al., 2016). Lithological and mineralogical characteristics of the study sections indicate that the strata underwent insignificant metamorphism in the geologic history, implying minor metamorphic alteration on the $\delta^{15}\text{N}$ signature of our samples (Chang et al., 2016, 2017, 2018).

As diagenetic and metamorphic alterations are bound to the loss of C and/or N from sedimentary organic matter, plots of $\delta^{15}\text{N}$ –TN, $\delta^{15}\text{N}$ –TOC, and $\delta^{15}\text{N}$ –C/N were commonly used to evaluate the preservation of primary $\delta^{15}\text{N}$ signatures (Cremonese et al., 2013, 2014; Ader et al., 2014; Wang et al., 2015, 2018a; Wang et al., 2018b). For example, a decrease in N content is often coupled to increasing $\delta^{15}\text{N}$ values at metamorphic grades higher than greenschist facies, indicative of significant alteration of $\delta^{15}\text{N}$ during metamorphism (Ader et al., 2014, 2016). The lack of evident correlations in the $\delta^{15}\text{N}$ –TN (Figs. 5D and 6D), $\delta^{15}\text{N}$ –TOC (Figs. 5E and 6E), and $\delta^{15}\text{N}$ –C/N (Figs. 5F and 6F) plots also demonstrate that primary N isotopic compositions have not been modified significantly. Therefore, the $\delta^{15}\text{N}$ signatures are likely to reflect oceanic biogeochemical processes during the Cambrian Stage 4.

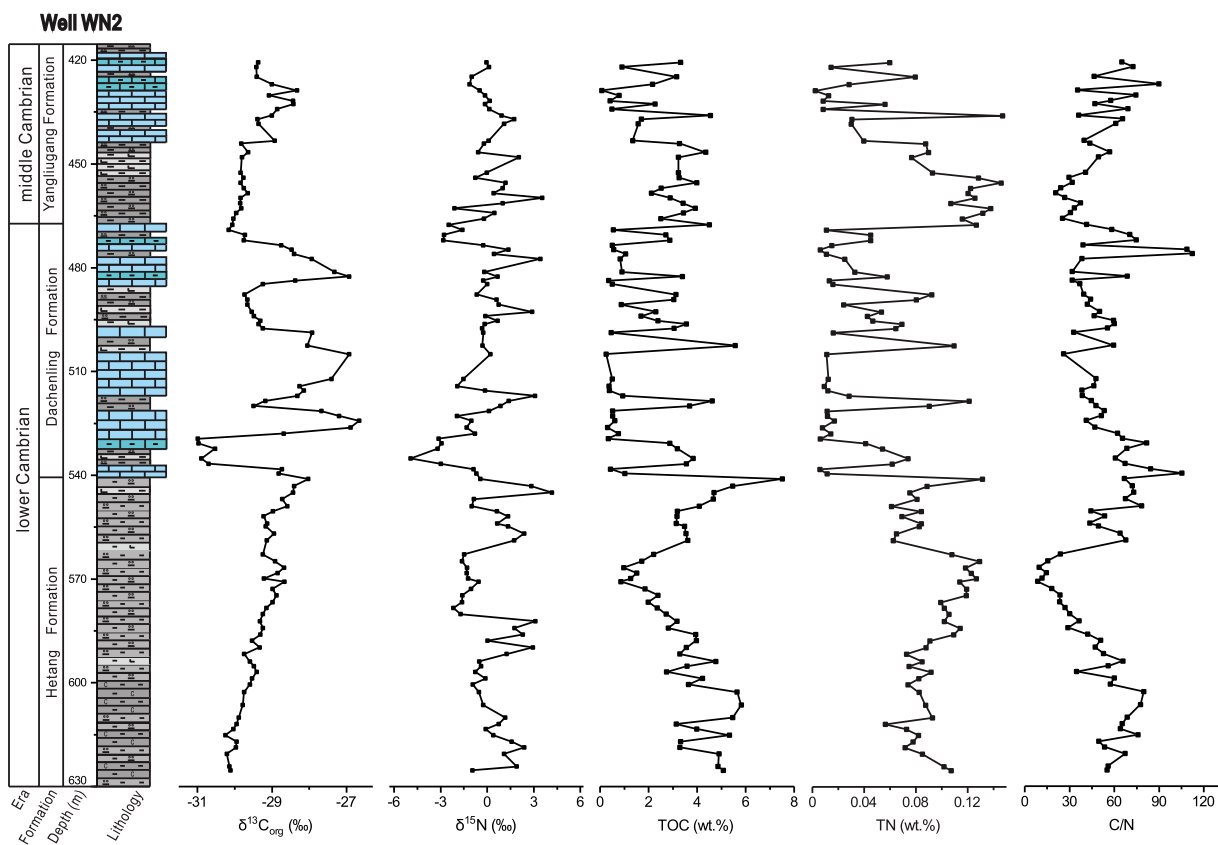


Fig. 4. Chemostratigraphic column of the Well WN2 section.

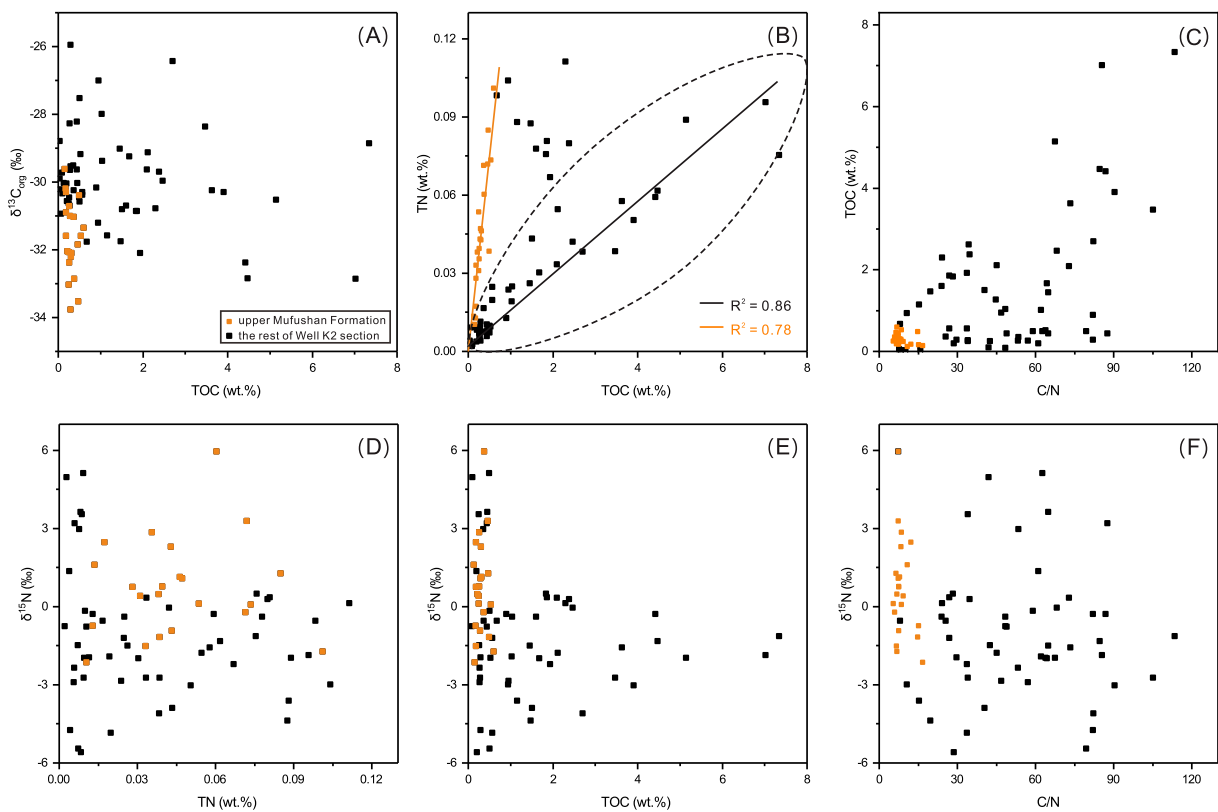


Fig. 5. Data plots for Well K2 section: (A) $\delta^{13}\text{C}_{\text{org}}$ -TOC; (B) TN-TOC; (C) TOC-C/N; (D) $\delta^{15}\text{N}$ -TN; (E) $\delta^{15}\text{N}$ -TOC; (F) $\delta^{15}\text{N}$ -C/N.

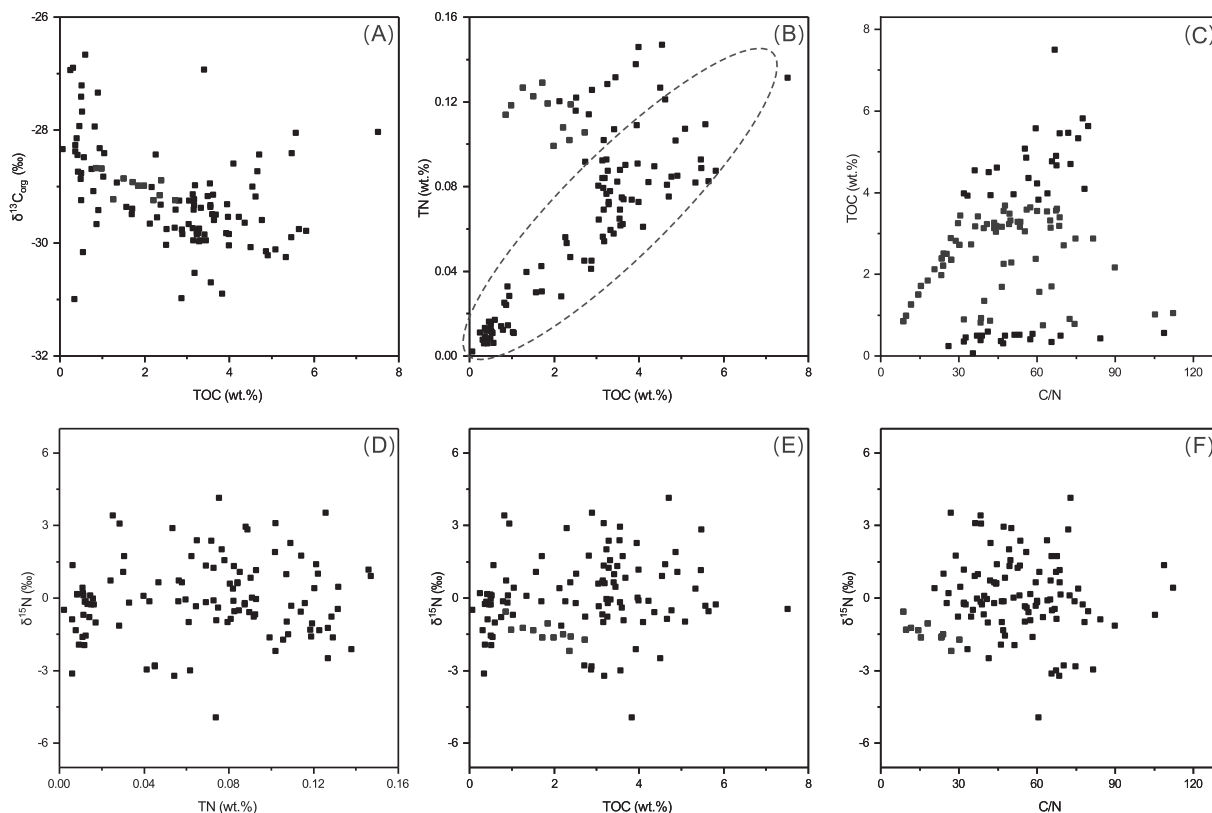


Fig. 6. Data plots for Well WN2 section: (A) $\delta^{13}\text{C}_{\text{org}}$ -TOC; (B) TN-TOC; (C) TOC-C/N; (D) $\delta^{15}\text{N}$ -TN; (E) $\delta^{15}\text{N}$ -TOC; (F) $\delta^{15}\text{N}$ -C/N.

5.2. Stratigraphic correlation

Secular variations of seawater C isotopic signatures are controlled by changes in the long-term input of carbon to the ocean and its partitioning into organic and inorganic reservoirs (Kump and Arthur, 1999; Zhu et al., 2004). Extensive C isotopic studies have established regional and global chemostratigraphic frameworks that can be used for stratigraphic correlation during the Ediacaran–Cambrian transition (Brasier et al., 1994; Zhu et al., 2006, 2018; Maloof et al., 2010).

The generalized $\delta^{13}\text{C}_{\text{carb}}$ curve through the Cambrian proposed in Zhu et al. (2006) was commonly referred to in previous chemostratigraphic correlation works, especially those concerning the Cambrian strata in South China and Australia (Guo et al., 2010; Wang et al., 2011; Li et al., 2013; Ishikawa et al., 2014; Faggetter et al., 2016; Chang et al., 2017; Betts et al., 2018). According to the curve, one positive and two negative carbon isotope excursions occurred during the Cambrian Stage 4, i.e., the MIngxinsi Carbon Isotope Excursion (MICE) during the early Cambrian Stage 4, the Archaeocyathid Extinction Carbon isotope Excursion (AECE) during the middle Cambrian Stage 4, and the Redlichiid–Olenellid Extinction Carbon isotope Excursion (ROECE) during the terminal Cambrian Stage 4.

Lately, a revised Cambrian stratigraphic scheme was proposed and the AECE was suggested as a marker to identify the base of the Cambrian Stage 4 (Zhu et al., 2018). In

this case, the Cambrian Epoch 2 is divided into an early stage characterized by diversification of animals and a late stage characterized by mass extinctions (Zhu et al., 2018). The upper boundary can be identified by the ROECE, which has been reported from both the Gondwana and Laurentia continents (Montañez et al., 2000; Zhu et al., 2004; Guo et al., 2010; Wang et al., 2011; Faggetter et al., 2016), and occurs at the base of the Wuliuan Stage (Stage 5) on the newly ratified stratotype section for the base of the Miaolingian Series (Cambrian Series 3) and Wuliuan Stage (IUGS E-Bulletin#144; Zhao et al., 2007; Zhu et al., 2018).

The MICE, AECE, and ROECE were identified on the $\delta^{13}\text{C}_{\text{carb}}$ curve of the Mufushan Formation in Well K2, while the AECE and ROECE were identified on the $\delta^{13}\text{C}_{\text{carb}}$ curve of the Dachenling Formation in Well WN2 in Chang et al. (2017). The former is constrained by the occurrence of *Hupeidiscus fengdongensis* at ~500 m and *Redlichia murakamii* at ~360 m in the Well K2 section (Zhang and Zhou, 1985; Zhu et al., 2004, 2018; Zuo et al., 2008; Chang et al., 2017); whereas the latter is supported by occurrences of *Redlichia* (*Pteroredlichia*) *chinesis* across the whole Dachenling Formation in adjacent areas (Dongzhi area; Zhu et al., 2004, 2005; Kouchinsky et al., 2012; Chang et al., 2017). A lack of carbonate-bearing strata precludes the possibility of obtaining $\delta^{13}\text{C}_{\text{carb}}$ data for the Hetang Formation in Well WN2 (Fig. 2B). However, the $\delta^{13}\text{C}_{\text{org}}$ plot of Well WN2 includes a positive excursion from the upper Hetang Formation to the bottom

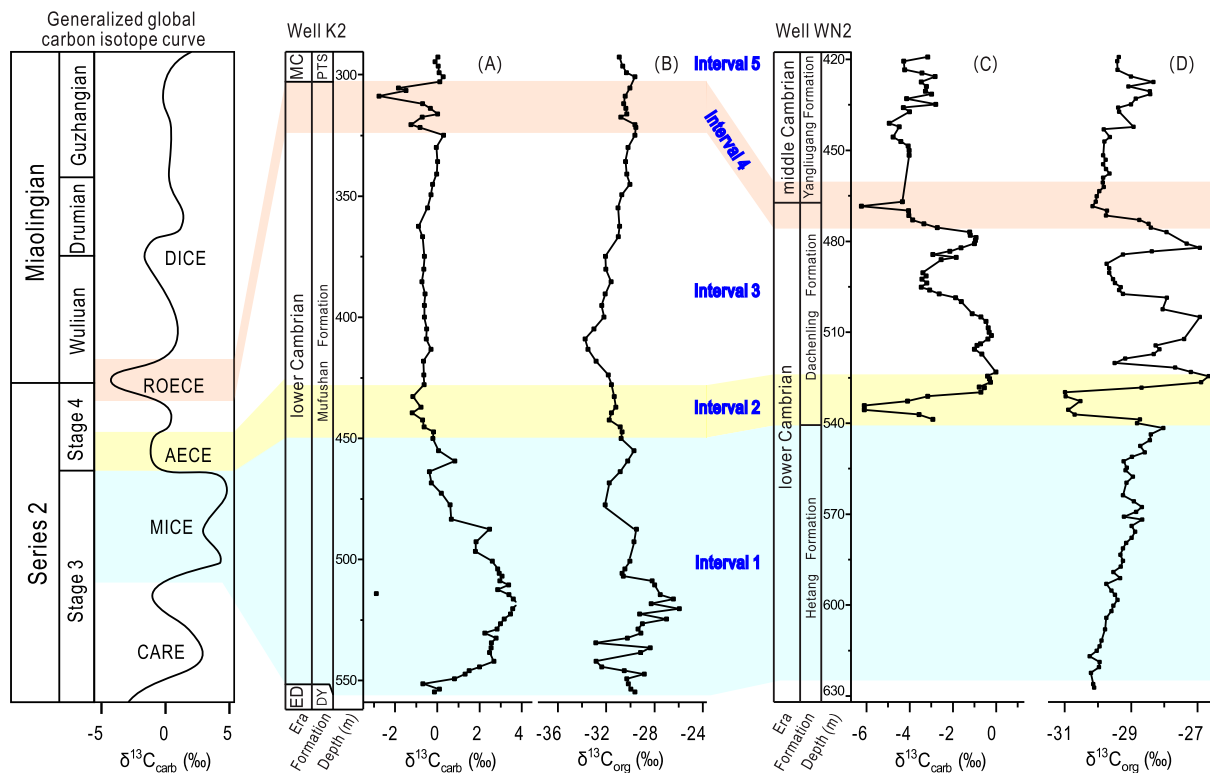


Fig. 7. Carbon isotope stratigraphic correlations in the Well K2 and WN2 sections: (A) $\delta^{13}\text{C}_{\text{carb}}$ plot of the Well K2 section; (B) $\delta^{13}\text{C}_{\text{org}}$ plot of the Well K2 section; (C) $\delta^{13}\text{C}_{\text{carb}}$ plot of the Well WN2 section; (D) $\delta^{13}\text{C}_{\text{org}}$ plot of the Well WN2 section. The generalized C isotope curve was modified from Zhu et al. (2006).

of the Dachenling Formation (Fig. 4). According to the generalized Cambrian C isotope curve (Zhu et al., 2006, 2018), this excursion can be tentatively correlated with the MICE. This correlation is supported by the occurrence of *Hupeidiscus orientalis* in the upper Hetang Formation at Anji, Zhejiang Province (Fig. 1B; Yang et al., 2008; Zhu et al., 2018).

Taking the AECE as the marker for the base of the Cambrian Stage 4, the stratigraphic correlation result of the study sections can be summarized in Fig. 7. The strata of the Cambrian Stage 4 cover the middle to the top part of the Mufushan Formation in Well K2, and the whole Dachenling Formation in Well WN2. Overall, both Well K2 and WN2 sections can be divided into five intervals based on carbon isotope stratigraphy (Fig. 7). Intervals 1, 2, and 4 correspond to MICE, AECE, and ROECE C isotope excursion events, respectively; intervals 3 and 5 correspond to the stages before and after ROECE, respectively. Nitrogen cycling during different intervals are discussed below on the basis of N isotopic signatures.

5.3. Explanation of nitrogen isotopic signatures

5.3.1. Interval 1

In Interval 1, the Well K2 section is characterized by a significant negative $\delta^{15}\text{N}$ excursion overlapping with a strong positive carbon isotope excursion (Fig. 8A, B). $\delta^{15}\text{N}$ values of $<-4\text{‰}$ can result from either nitrogen fixa-

tion with V- or Fe-based nitrogenase enzymes or anaerobic assimilation of NH_4^+ (Kappler et al., 2005; Crowe et al., 2008; Higgins et al., 2012; Zhang et al., 2014; Stüeken et al., 2016). However, the former requires a lack of Mo-based nitrogenase enzymes in diazotrophs, countering the expanded Mo reservoir during this stage (Xiang et al., 2017). Therefore, the negative $\delta^{15}\text{N}$ excursion was likely caused by enhanced assimilation of NH_4^+ in anoxic water column. High TOC contents during this interval supports that the anoxia might be associated with high primary productivity and increased oxygen consumption during degradation of organic matter (Fig. 3). With the decrease of TOC contents, $\delta^{15}\text{N}$ values increase from $<-4\text{‰}$ to $>+3\text{‰}$, reflecting enhanced denitrification/anammox and reoxygenation of the water column (Ader et al., 2014, 2016; Stüeken et al., 2016; Wang et al., 2018a). With the increase of TOC contents, $\delta^{15}\text{N}$ values decrease to $<+1\text{‰}$ at the top of Interval 1 (Figs. 3 and 8A), indicating that anoxia might have expanded again due to increased oxygen consumption.

During Interval 1, the Well WN2 section displays several positive $\delta^{15}\text{N}$ excursions (Fig. 8C). Iron speciation and trace element analysis results reflected a stratified ocean redox structure and expanded oxygenation toward the anoxic deep ocean during this stage (Jin et al., 2016; Li et al., 2017; Xiang et al., 2017). Therefore, the positive $\delta^{15}\text{N}$ excursions with peak $\delta^{15}\text{N}$ values of $>+2\text{‰}$ were likely associated with enhanced denitrification/anammox caused by increased oxygenation of the water column

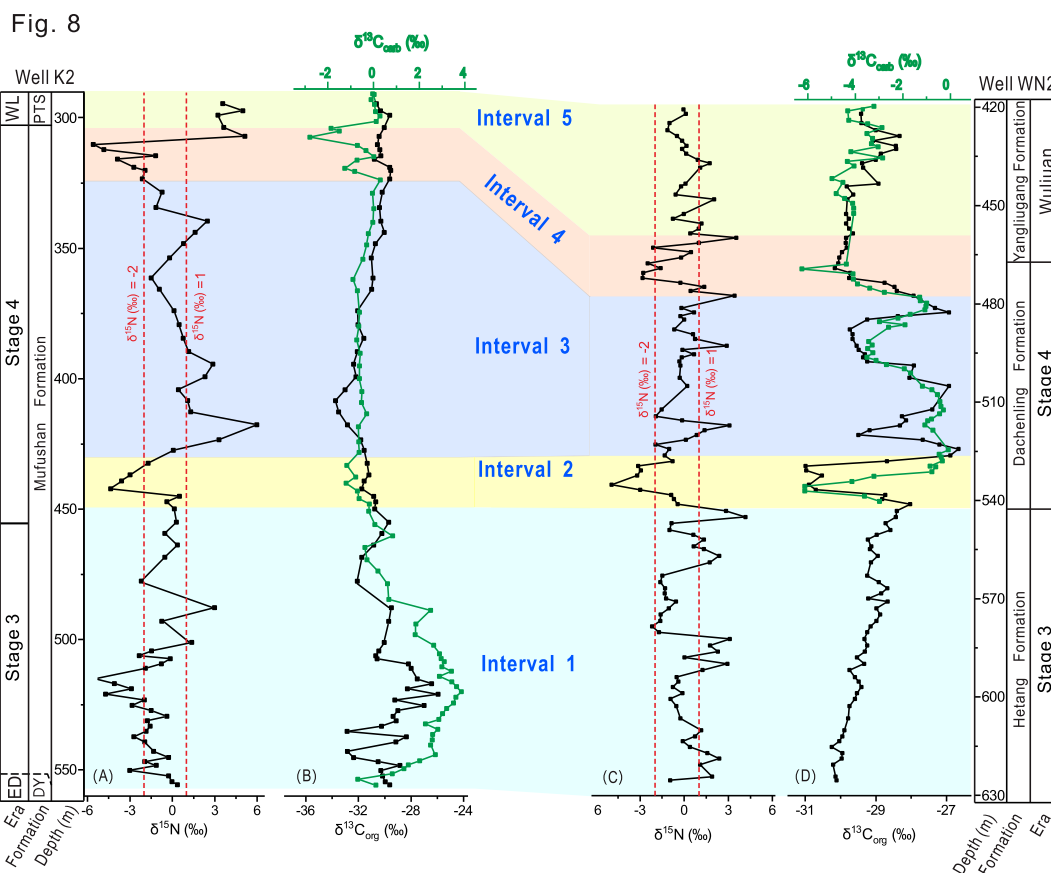


Fig. 8. $\delta^{15}\text{N}$, $\delta^{13}\text{C}_{\text{carb}}$, and $\delta^{13}\text{C}_{\text{org}}$ profiles of the Well K2 and WN2 sections: (A) $\delta^{15}\text{N}$ profile of the Well K2 section; (B) $\delta^{13}\text{C}_{\text{org}}$ profile of the Well K2 section; (C) $\delta^{15}\text{N}$ profile of the Well WN2 section; (D) $\delta^{13}\text{C}_{\text{org}}$ profile of the Well WN2 section.

(Wang et al., 2015, 2018a). In contrast, the low $\delta^{15}\text{N}$ values likely reflect an anaerobic nitrogen cycle with active NH_4^+ assimilation, and quantitative consumption of NO_3^- by chemocline denitrification/anammox (Higgins et al., 2012; Stüeken, 2013).

5.3.2. Intervals 2 and 3

In Interval 2, both Well K2 and WN2 sections are characterized by a strong negative $\delta^{15}\text{N}$ excursion as well as negative $\delta^{13}\text{C}_{\text{carb}}$ and $\delta^{13}\text{C}_{\text{org}}$ excursions (Fig. 8). According to the stratigraphic correlation result, the N and C isotope excursions coincide with a major transgression and a widespread anoxic event (i.e., the Sinsk event) that has been identified across the Siberian and Yangtze platforms (Zhuravlev and Wood, 1996). This is consistent with the lithological transition from limestone to black shale during Interval 2 in both of the sections (Figs. 3, 4 and 8). Therefore, the negative $\delta^{15}\text{N}$ excursion was most likely caused by anaerobic assimilation of NH_4^+ associated with widespread anoxia in the shallow ocean (Higgins et al., 2012).

The subsequent increase in $\delta^{15}\text{N}$ values during the Intervals 2–3 transition reflect enhanced denitrification/anammox and increased O_2 availability in the water column (Fig. 8A and C). This process coincides with the lithological transition from black shale to limestone, which can be attributed to the regression of the ocean following the

transgression. Therefore, the increasing $\delta^{15}\text{N}$ values were likely caused by re-oxygenation of the water column associated with the regression. The $\delta^{15}\text{N}$ values increase up to $> +3\text{‰}$ in both Well K2 and WN2 sections, demonstrating that a dominantly oxic water column finally developed across the shallow ocean during this process (Ader et al., 2016; Stüeken et al., 2016). This is consistent with the iron speciation data reported in Li et al. (2017).

In Interval 3, both Well K2 and WN2 sections are dominated by $\delta^{15}\text{N}$ values ranging from -2‰ to $+1\text{‰}$ (Fig. 8A, C). This $\delta^{15}\text{N}$ signature can result from one of the three scenarios: (1) a completely oxic ocean with all denitrification restricted to sediments; (2) a nitrogen cycle with quantitative denitrification across the redox gradient in the water column; (3) N_2 fixation as the primary nitrogen source for the local biota (Stüeken, 2013; Ader et al., 2014, 2016). The first scenario is inconsistent with an anoxic deep ocean reflected by iron speciation data during this stage (Xiang et al., 2017), while the second scenario contradicts with an oxic shallow ocean revealed by the nitrogen isotope signatures in this study. Therefore, it is highly plausible that the $\delta^{15}\text{N}$ values ranging from -2‰ to $+1\text{‰}$ are reflective of an aerobic nitrogen cycle dominated by N_2 fixation.

Notably, two positive $\delta^{15}\text{N}$ excursions co-occur with negative $\delta^{13}\text{C}_{\text{carb}}$ and $\delta^{13}\text{C}_{\text{org}}$ excursions as well as litholog-

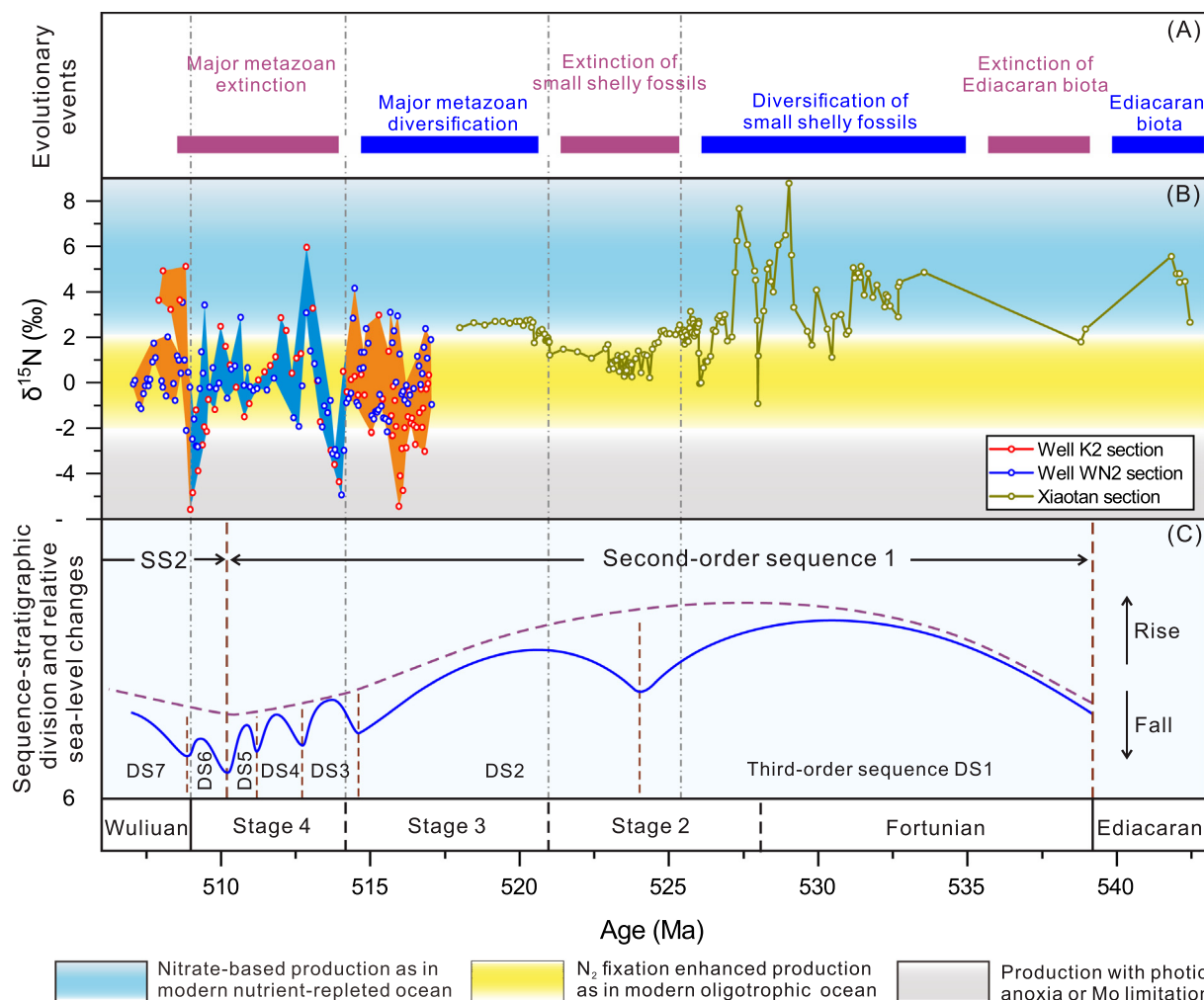


Fig. 9. Diagram showing (A) evolutionary events (modified after Wang et al., 2018a); (B) nitrogen isotope signatures from terminal Ediacaran to early Cambrian Stage 5; (C) sequence-stratigraphic division and sea-level changes (modified after Mei et al., 2007). Nitrogen isotope data of the Xiaotan section was cited from Cremonese et al. (2013).

ical changes from limestone to black shale in Interval 3 in Well WN2 section, while no corresponding isotopic and lithological variations can be identified in the Well K2 section. This phenomenon can be well explained by small-scale transgression–regression processes. During the transgression, the chemocline would have risen as a result of upwelled anoxic deep water or enhanced oxygen consumption by degradation of organic matter (Zhuravlev and Wood, 1996). As a result, denitrification/anammox would have been intensified in the dominantly oxic water column, leading to higher $\delta^{15}\text{N}$ values in the remaining N species (Cremonese et al., 2013; Higgins et al., 2012; Stüeken et al., 2016).

5.3.3. Intervals 4 and 5

In Interval 4, a strong negative $\delta^{15}\text{N}$ excursion occurs with negative $\delta^{13}\text{C}_{\text{carb}}$ and $\delta^{13}\text{C}_{\text{org}}$ excursions in both sections, resembling those of Interval 2 (Fig. 8). Similarly, the negative $\delta^{15}\text{N}$ excursion can be attributed to enhanced anoxia in the shallow ocean.

An increase in $\delta^{15}\text{N}$ values occurs during the Intervals 4–5 transition in both sections (Fig. 8A, C), reflecting re-oxygenation of the water column. $\delta^{15}\text{N}$ values in the Well K2 section are maintained at values above +3‰ in Interval 5, reflecting the development of a stable oxic water column (Ader et al., 2014, 2016; Stüeken et al., 2016). In contrast, $\delta^{15}\text{N}$, $\delta^{13}\text{C}_{\text{org}}$, and $\delta^{13}\text{C}_{\text{carb}}$ values in Well WN2 remain low in Interval 5 (Figs. 4 and 8C, D). The N and C isotopic gradients collectively reflect enhanced redox stratification of the ocean during this stage (Jiang et al., 2007; Stüeken, 2013; Wang et al., 2014, 2016), which was possibly associated with the eruption of the Kalkarindji Large Igneous Province of northern Australia (Hough et al., 2010; Jourdan et al., 2014).

5.4. Implications for ocean chemistry during the Cambrian Stage 4

The major metazoan extinction during the Cambrian Stage 4 has been attributed to anoxic events associated with

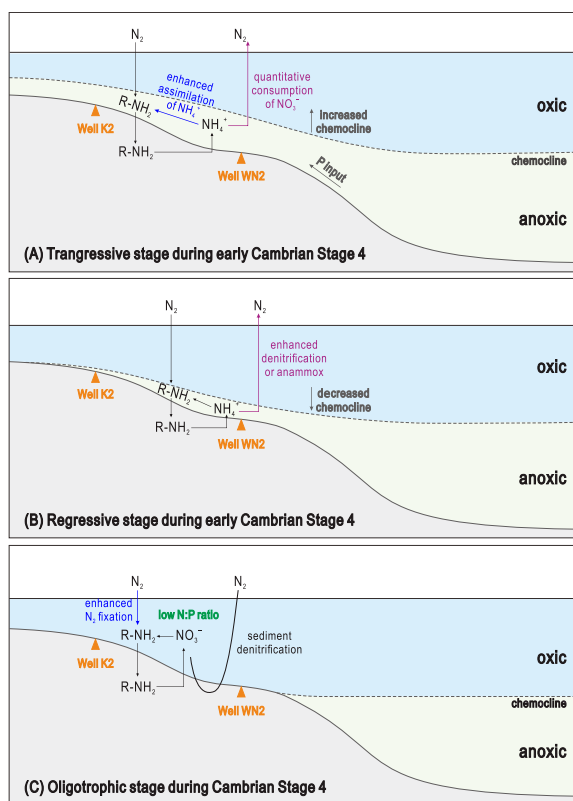


Fig. 10. Schematic model of the evolution of the nitrogen cycle and oceanic redox structure in the shallow ocean during Cambrian Stage 4: (A) Transgressive stage during early Cambrian Stage 4. Photic anoxia occurred as a result of intense transgression and NO_3^- was quantitatively consumed through denitrification or anammox. Assimilation of ^{15}N -depleted NH_4^+ by primary producers enhanced in the anoxic water column. Large amounts of P was transported to the shallow ocean; (B) Regressive stage during early Cambrian Stage 4. The water column in the shallow ocean was re-oxidized as a result of regression. The oxidation of NH_4^+ produced NO_3^- or NO_2^- , which then reacted with the remaining NH_4^+ in the anoxic water through denitrification or anammox, leading to significant N loss from the ocean and enrichment of ^{15}N in the remaining nitrogen reservoir; (C) Oligotrophic stage during Cambrian Stage 4. Significant N loss and P input resulted in low N:P ratios and severe N limitation in the shallow ocean. N_2 fixation by diazotroph enhanced to complement the N supply to the ocean.

large-amplitude eustatic changes or global volcanic activities in previous studies (Zhuravlev and Wood, 1996; Hough et al., 2010; Jourdan et al., 2014; Nielsen and Schovsbo, 2015; Zhu et al., 2018). Nitrogen isotope data in this study demonstrated widespread anaerobic assimilation of NH_4^+ in the shallow ocean during the early and terminal Cambrian Stage 4, lending new support to a possible link between anoxia and the extinction event. On the other hand, however, both the nitrogen isotope data in this study and iron speciation results reported in Li et al. (2017) indicated that the shallow ocean was dominantly oxic for the rest of the Cambrian Stage 4, arguing against anoxia as the sole cause for the prolonged substantial decline of metazoan diversity throughout this stage.

Interestingly, nitrogen isotope signatures in this study indicated that the oxic shallow ocean was characterized by a nitrogen cycle with strong N_2 fixation. Due to high energy cost of breaking N–N chemical bonds, nitrogen fixation normally increases only when concentrations of other nitrogen species, such as NH_4^+ or NO_3^- , are inadequate in the water column (Tyrrell, 1999; Kikumoto et al., 2014; Wang et al., 2019). For example, in the low-latitude oligotrophic oceans such as the North Atlantic Ocean, N_2 fixation makes a major contribution to the nitrogen budget, in response to N depletion in the water column (Montoya et al., 2002, 2004). As a result, near-surface organic matter in the ocean is characterized by low $\delta^{15}\text{N}$ values close to 0, similar to those of the Cambrian Stage 4 strata studied in this work. Therefore, the nitrogen isotope signatures are likely indicative of an oligotrophic environment in the shallow ocean during most of the Cambrian Stage 4. Notably, complication of nitrogen isotope data from sediments across the modern ocean demonstrated that $\delta^{15}\text{N}$ values close to 0 are quite rare, even in the low-latitude oligotrophic oceans dominated by N_2 fixation (Tesdal et al., 2013; Wang et al., 2019). The major cause behind the increase of $\delta^{15}\text{N}$ at the seafloor is likely the loss of ^{15}N -depleted components through oxic diagenesis in these settings (Tesdal et al., 2013). Preservation of primary $\delta^{15}\text{N}$ values in the study sections may be associated with high sedimentation rates that slowed down diagenetic alteration (Robinson et al., 2012), evidenced by increased terrestrial input during this stage (Montañez et al., 2000). More importantly, the impact of oxic diagenesis on sedimentary $\delta^{15}\text{N}$ records may have weakened significantly during the early Cambrian due to low oxygen levels in the ocean and atmosphere (10–40% present atmospheric level; Sperling et al., 2015).

In an oligotrophic ocean, low N concentrations can limit the growth rate of individual cells and the total biomass will also be restricted to a low level (Moore et al., 2013). Furthermore, eukaryotes preferentially assimilate NO_3^- over NH_4^+ compared with prokaryotes (Fawcett et al., 2011). For example, in the oligotrophic Sargasso Sea, the eukaryotes are more reliant on the external NO_3^- supply from the deep ocean, whereas the prokaryotes rely mostly on the recycled NH_4^+ in the surface ocean (Fawcett et al., 2011). As a result, the development of eukaryotes will be more severely hindered in an oligotrophic ocean. Eukaryotes serve as an essential food source for metazoans at higher tropic levels in the food chain (e.g., Brocks et al., 2017; Wang et al., 2018a). Therefore, the sustained N-limited oligotrophic environment could have significantly hampered the development of eukaryotes in the shallow ocean, which in turn contributed to the prolonged substantial decline of metazoan diversity during the Cambrian Stage 4.

An important concern about the oligotrophy–extinction scenario is whether the oligotrophic environment was restricted to the studied area or occurred globally in the shallow ocean. To answer this question, it is essential to figure out the mechanism for the development of prolonged oligotrophy during the Cambrian Stage 4.

During the Cambrian Stages 1–3, several pulses of expanded NO_3^- reservoirs were revealed by positive N iso-

tope signatures in the shallow ocean, coinciding with the radiation of animals (Fig. 9A and B; Wang et al., 2018a). Nitrogen isotope signatures in this study were also consistent with increased NO_3^- supply from expanded oxygenation toward the anoxic deep ocean during the late Cambrian Stage 3. However, at the start of the Cambrian Stage 4, anaerobic assimilation of NH_4^+ became prevalent in the shallow ocean, implying that NO_3^- in the water column had been quantitatively consumed through denitrification or anammox (Fig. 10A and 11A). This anoxic event has been identified across the Siberian and Yangtze platforms as well as in Canada and Australia (Zhuravlev and Wood, 1996; Dilliard et al., 2007; Hall, 2012), and was likely caused by a major transgressive event during this stage (Fig. 9C; Zhuravlev and Wood, 1996; Mei et al., 2007).

Subsequent oxygenation of the shallow ocean during the regression was characterized by increasing nitrogen isotope signatures reflective of intense denitrification/anammox (Figs. 9A and 10B). During this process, significant amounts of N would have been lost from the ocean through the release of N_2 or N_2O to the atmosphere, contributing to N limitation and enhanced N_2 fixation (Ganeshram et al., 2000, 2002; Horikawa et al., 2006). In addition, large amounts of P would have been released through denitrification and anammox processes (Moore et al., 2013). Combined with strong input of P through upwelling during the transgressive stage (Fig. 10A; Zhuravlev and Wood, 1996), N:P ratios of the water column would have reached a level much lower than the Redfield ratio (i.e., 16:1), aggravating N limitation in the shallow ocean (Figs. 9A and 10C). Similar processes have been used in previous studies to explain the development of N-limited environments during the Cretaceous oceanic anoxic events and early Triassic (Kuypers et al., 2004; Grasby et al., 2016).

Compared with the Cambrian Stages 1–3, the Cambrian Stage 4 was characterized by more frequent eustatic fluctuations (Fig. 9C). During small-scale transgression–regression cycles, the introduction of anoxic deep water and enhanced O_2 consumption through degradation of organic matter would lead to increased chemocline in the shallow ocean (Fig. 10C). As a result, denitrification/anammox would have enhanced in the water column. Large amounts of N would have been released to the atmosphere during this process, resulting in decreased N:P ratios and aggravated N limitation in the seawater. Therefore, frequent eustatic fluctuations could have facilitated the persistence of the oligotrophic environment in the shallow ocean during the Cambrian Stage 4. This scenario is consistent with the variations of lithology and N isotope signatures in the Well WN2 section (see Section 5.3.2 for detailed discussion).

In summary, it is suggested that the oligotrophic environment in the shallow ocean initially resulted from the major anoxic event during the early Cambrian 4 and was maintained through frequent eustatic fluctuations in the rest of the Cambrian Stage 4. Both the anoxic event and eustatic fluctuations have been identified to be a global phenomenon in previous studies (Zhuravlev and Wood, 1996;

Dilliard et al., 2007; Mei et al., 2007; Hall, 2012; Peng et al., 2012; Nielsen and Schovsbo, 2015; Zhu et al., 2018). Therefore, it is reasonable to conclude that the oligotrophic environment was widespread in the global shallow ocean during the Cambrian Stage 4 and played an important role in the prolonged substantial decline of metazoan diversity during this stage. Further nitrogen isotope studies in other areas will help to test the scenario and lead to a better understanding of the possible link between the variation of nitrogen supply and the biotic crisis event.

6. CONCLUSIONS

Nitrogen isotopic signatures of the Well K2 and WN2 sections revealed important information about the biogeochemical cycle during the Cambrian Stage 4.

During the early and terminal Cambrian Stage 4, the shallow ocean was characterized by highly negative $\delta^{15}\text{N}$ values, indicative of anaerobic assimilation of NH_4^+ in the water column. The results lend new support to the traditional view that expanded anoxia contributed to the extinction of metazoan during the Cambrian Stage 4.

More importantly, the nitrogen isotopic signatures demonstrated that oligotrophic environment characterized by strong N limitation prevailed in the shallow ocean during the Cambrian Stage 4. The oligotrophic environment was likely caused by aggravated N loss as well as enhanced P input during eustatic changes, and may have been widely distributed in the global shallow ocean. The adverse environment could have hindered the development of eukaryotes, which in turn led to the breakdown of the entire food chain and contributed to the prolonged substantial decline of metazoan diversity during this stage.

ACKNOWLEDGEMENTS

Great thanks to two reviewers: Thomas Algeo and Eva E. Stüeken, for their constructive comments that helped improve the manuscript. We are also grateful to the editor for handling our manuscript. This study was financially supported by the National Key Research and Development Program (Grant No. 2017YFC0603101), National Natural Science Foundation of China (Grant No. 41802026, 41830425, 41890845, and 41621003), China Postdoctoral Science Foundation (Grant No. 2018M633553), 111 Project (D17013), and the Strategic Priority Research Program of Chinese Academy of Sciences (Grant No. XDB26000000).

REFERENCES

- Ader M., Macouin M., Trindade R. I. F., Hadrien M. H., Yang Z., Sun Z. and Besse J. (2009) A multilayered water column in the Ediacaran Yangtze platform? Insights from carbonate and organic matter paired $\delta^{13}\text{C}$. *Earth Planet. Sci. Lett.* **288**, 213–227.
- Ader M., Sansjofre P., Halverson G. P., Busigny V., Trindade R. I. F., Kunzmann M. and Nogueira A. C. R. (2014) Ocean redox structure across the Late Neoproterozoic Oxygenation Event: A nitrogen isotope perspective. *Earth Planet. Sci. Lett.* **396**, 1–13.
- Ader M., Thomazo C., Sansjofre P., Busigny V., Papineau D., Laffont R., Cartigny P. and Halverson G. P. (2016) Interpre-

- tation of the nitrogen isotopic composition of Precambrian sedimentary rocks: Assumptions and perspectives. *Chem. Geol.* **429**, 93–110.
- Altabet M. A., Pilskaln C., Thunell R., Pride C., Sigman D., Chavez F. and Francois R. (1999) The nitrogen isotope biogeochemistry of sinking particles from the margin of the Eastern North Pacific. *Deep Sea Res. Part I* **46**, 655–679.
- Bebout G. E. (1997) Nitrogen isotope tracers of high-temperature fluid-rock interactions: Case study of the Catalina Schist, California. *Earth Planet. Sci. Lett.* **151**, 77–90.
- Bekker A., Holmden C., Beukes N. J., Kenig F., Eglington B. and Patterson W. P. (2008) Fractionation between inorganic and organic carbon during the Lomagundi (2.22–2.1 Ga) carbon isotope excursion. *Earth Planet. Sci. Lett.* **271**, 278–291.
- Benton M. J. (1995) Diversification and extinction in the history of life. *Science* **268**, 52–58.
- Betts M. J., Paterson J. R., Jacquet S. M., Andrew A. S., Hall P. A., Jago J. B., Jagodzinski E. A., Preiss W. V., Crowley J. L. and Brougham T. (2018) Early Cambrian chronostratigraphy and geochronology of South Australia. *Earth-Sci. Rev.* **185**, 498–543.
- Brasier M. D. (1992) Nutrient-enriched waters (NEW) and the early skeletal fossil record. *J. Geol. Soc.* **149**, 621–629.
- Brasier M. D., Corfield R. M., Derry L. A., Rozanov A. Y. and Zhuravlev A. Y. (1994) Multiple $\delta^{13}\text{C}$ excursions spanning the Cambrian explosion to the Botomian crisis in Siberia. *Geology* **22**, 455–458.
- Brocks J. J., Jarrett A. J., Sirantoine E., Hallmann C., Hoshino Y. and Liyanage T. (2017) The rise of algae in Cryogenian oceans and the emergence of animals. *Nature* **548**, 578.
- Cai C., Xiang L., Yuan Y., He X., Chu X., Chen Y. and Xu C. (2015) Marine C, S and N biogeochemical processes in the redox-stratified early Cambrian Yangtze ocean. *J. Geol. Soc.* **172**, 895–903.
- Calvert S. E. (2004) Beware intercepts: interpreting compositional ratios in multi-component sediments and sedimentary rocks. *Org. Geochem.* **35**, 981–987.
- Chang C., Hu W., Fu Q., Cao J., Wang X. and Yao S. (2016) Characterization of trace elements and carbon isotopes across the Ediacaran-Cambrian boundary in Anhui Province, South China: Implications for stratigraphy and paleoenvironment reconstruction. *J. Asian Earth Sci.* **125**, 58–70.
- Chang C., Hu W., Wang X., Yu H., Yang A., Cao J. and Yao S. (2017) Carbon isotope stratigraphy of the lower to middle Cambrian on the eastern Yangtze Platform, South China. *Palaeogeogr., Palaeoclimatol. Palaeoecol.* **479**, 90–101.
- Chang C., Hu W., Fu Q., Cao J., Wang X., Wan Y. and Yao S. (2018) Characteristics and formation processes of (Ba, K, NH_4)-feldspar and cymrite from a lower Cambrian black shale sequence in Anhui Province, South China. *Mineral. Mag.* **82**, 1–21.
- Chu D., Liu J. and Wang C. (2016) An updated stratigraphy subdivision of the Cambrian system in Anhui Province. *J. Stratigraphy* **40**, 85–91.
- Cloud P. E. (1948) Some problems and patterns of evolution exemplified by fossil invertebrates. *Evolution* **2**, 322–350.
- Cook P. J. (1992) Phosphogenesis around the Proterozoic-Phanerozoic transition. *J. Geol. Soc.* **149**, 615–620.
- Cook P. J. and Shergold J. H. (1984) Phosphorus, phosphorites and skeletal evolution at the Precambrian-Cambrian boundary. *Nature* **308**, 231–236.
- Cremonese L., Shields-Zhou G. A., Struck U., Ling H., Och L., Chen X. and Li D. (2013) Marine biogeochemical cycling during the early Cambrian constrained by a nitrogen and organic carbon isotope study of the Xiaotan section, South China. *Precambrian Res.* **225**, 148–165.
- Cremonese L., Shields-Zhou G. A., Struck U., Ling H. and Och L. M. (2014) Nitrogen and organic carbon isotope stratigraphy of the Yangtze Platform during the Ediacaran-Cambrian transition in South China. *Palaeogeogr., Palaeoclimatol. Palaeoecol.* **398**, 165–186.
- Crowe S. A., Jones C., Katsev S., Magen C., O'Neill A. H., Sturm A., Canfield D. E., Haffner G. D., Mucci A. and Sundby B. (2008) Photoferrotrophs thrive in an Archean Ocean analogue. *Proc. Natl. Acad. Sci.* **105**, 15938–15943.
- Dilliard K. A., Pope M. C., Coniglio M., Hasiotis S. T. and Lieberman B. S. (2007) Stable isotope geochemistry of the lower Cambrian Sekwi Formation, Northwest Territories, Canada: Implications for ocean chemistry and secular curve generation. *Palaeogeogr., Palaeoclimatol. Palaeoecol.* **256**, 174–194.
- Faggetter L. E., Wignall P. B., Pruss S. B., Newton R. J., Sun Y. and Crowley S. (2017) Trilobite extinctions, facies changes and the ROECE carbon isotope excursion at the Cambrian Series 2–3 boundary, Great Basin, western USA. *Palaeogeogr., Palaeoclimatol. Palaeoecol.* **478**, 53–66.
- Faggetter L. E., Wignall P. B., Pruss S. B., Sun Y., Raine R. J., Newton R. J., Widdowson M., Joachimski M. M. and Smith P. M. (2016) Sequence stratigraphy, chemostratigraphy and facies analysis of Cambrian Series 2 – Series 3 boundary strata in northwestern Scotland. *Geol. Mag.* **155**, 865–877.
- Fawcett S. E., Lomas M. W., Casey J. R., Ward B. B. and Sigman D. M. (2011) Assimilation of upwelled nitrate by small eukaryotes in the Sargasso Sea. *Nat. Geosci.* **4**, 717–722.
- Freudenthal T., Wagner T., Wenzhöfer F., Zabel M. and Wefer G. (2001) Early diagenesis of organic matter from sediments of the eastern subtropical Atlantic: evidence from stable nitrogen and carbon isotopes. *Geochim. Cosmochim. Acta* **65**, 1795–1808.
- Ganeshram R. S., Pedersen T. F., Calvert S. E., McNeill G. W. and Fontugne M. R. (2000) Glacial-interglacial variability in denitrification in the World's Oceans: Causes and consequences. *Paleoceanography* **15**, 361–376.
- Ganeshram R. S., Pedersen T. F., Stephen C. and Roger F. O. (2002) Reduced nitrogen fixation in the glacial ocean inferred from changes in marine nitrogen and phosphorus inventories. *Nature* **415**, 156–159.
- Grasby S. E., Beauchamp B. and Knies J. (2016) Early Triassic productivity crises delayed recovery from world's worst mass extinction. *Geology* **44**, 779–782.
- Guo Q., Strauss H., Liu C., Zhao Y., Yang X., Peng J. and Yang H. (2010) A negative carbon isotope excursion defines the boundary from Cambrian Series 2 to Cambrian Series 3 on the Yangtze Platform, South China. *Palaeogeogr., Palaeoclimatol. Palaeoecol.* **288**, 118–118.
- Guo Q., Strauss H., Zhu M., Zhang J., Yang X., Miao L. and Zhao F. (2013) High resolution organic carbon isotope stratigraphy from a slope to basinal setting on the Yangtze Platform, South China: Implications for the Ediacaran-Cambrian transition. *Precambrian Res.* **225**, 209–217.
- Hall P. A. (2012) *Elemental, Isotopic and Molecular Signatures of Early Cambrian Marine Sediments and a Phantom Petroleum System in South Australia*. University of Adelaide.
- Hayes J. M., Kaplan I. R. and Wedeking K. W. (1983) Precambrian organic geochemistry, preservation of the record. In *The Earth's Earliest Biosphere: Its Origin and Evolution* (ed. J. W. Schopf). Princeton University Press, Princeton, N.J., pp. 93–134.
- Higgins M. B., Robinson R. S., Husson J. M., Carter S. J. and Pearson A. (2012) Dominant eukaryotic export production during ocean anoxic events reflects the importance of recycled NH_4^+ . *Proc. Natl. Acad. Sci.* **109**, 2269–2274.
- Horikawa K., Minagawa M., Kato Y., Murayama M. and Nagao S. (2006) N_2 fixation variability in the oligotrophic Sulu Sea,

- western equatorial Pacific region over the past 83 kyr. *J. Oceanogr.* **62**, 427–439.
- Hough M. L., Shields G. A., Evins L. Z., Strauss H., Henderson R. A. and Mackenzie S. (2010) A major sulphur isotope event at c. 510 Ma: a possible anoxia–extinction–volcanism connection during the Early–Middle Cambrian transition? *Terra Nova* **18**, 257–263.
- Ishikawa T., Ueno Y., Shu D., Li Y., Han J., Guo J., Yoshida N., Maruyama S. and Komiya T. (2014) The $\delta^{13}\text{C}$ excursions spanning the Cambrian explosion to the Canglangpuian mass extinction in the Three Gorges area, South China. *Gondwana Res.* **25**, 1045–1056.
- Jiang G., Kaufman A. J., Christie-Blick N., Zhang S. and Wu H. (2007) Carbon isotope variability across the Ediacaran Yangtze platform in South China: Implications for a large surface-to-deep ocean $\delta^{13}\text{C}$ gradient. *Earth Planet. Sci. Lett.* **261**, 303–320.
- Jiang G., Wang X., Shi X., Xiao S., Zhang S. and Dong J. (2012) The origin of decoupled carbonate and organic carbon isotope signatures in the early Cambrian (ca. 542–520 Ma) Yangtze platform. *Earth Planet. Sci. Lett.* **317–318**, 96–110.
- Jin C., Li C., Algeo T. J., Planavsky N. J., Cui H., Yang X., Zhao Y., Zhang X. and Xie S. (2016) A highly redox-heterogeneous ocean in South China during the early Cambrian (~529–514Ma): Implications for biota-environment co-evolution. *Earth Planet. Sci. Lett.* **441**, 38–51.
- Jourdan F., Hodges K., Sell B., Schaltegger U., Wingate M. T. D., Evins L. Z., Söderlund U., Haines P. W., Phillips D. and Blenkinsop T. (2014) High-precision dating of the Kalkarindji large igneous province, Australia, and synchrony with the Early–Middle Cambrian (Stage 4–5) extinction. *Geology* **42**, 543–546.
- Kappler A., Pasquero C., Konhauser K. O. and Newman D. K. (2005) Deposition of banded iron formations by anoxygenic phototrophic Fe(II)-oxidizing bacteria. *Geology* **33**, 865–868.
- Kikumoto R., Tahata M., Nishizawa M., Sawaki Y., Maruyama S., Shu D., Han J., Komiya T., Takai K. and Ueno Y. (2014) Nitrogen isotope chemostratigraphy of the Ediacaran and Early Cambrian platform sequence at Three Gorges, South China. *Gondwana Res.* **25**, 1057–1069.
- Knoll A. H. and Carroll S. B. (1999) Early animal evolution: emerging views from comparative biology and geology. *Science* **284**, 2129–2137.
- Kouchinsky A., Bengtson S., Runnegar B., Skovsted C., Steiner M. and Vendrasco M. (2012) Chronology of Early Cambrian biomineralization. *Geol. Mag.* **149**, 221–251.
- Kump L. R. and Arthur M. A. (1999) Interpreting carbon-isotope excursions: carbonates and organic matter. *Chem. Geol.* **168**, 181–198.
- Kuypers M. M. M., Breugel Y. V., Schouten S., Erba E. and Damsté J. S. S. (2004) N_2 -fixing cyanobacteria supplied nutrient N for Cretaceous oceanic anoxic events. *Geology* **32**, 853–856.
- Lehmann M. F., Bernasconi S. M., Barbieri A. and Mckenzie J. A. (2002) Preservation of organic matter and alteration of its carbon and nitrogen isotope composition during simulated and in situ early sedimentary diagenesis. *Geochim. Cosmochim. Acta* **66**, 3573–3584.
- Leys S. P. and Kahn A. S. (2018) Oxygen and the energetic requirements of the first multicellular animals. *Integr. Comp. Biol.* **58**, 666–676.
- Li C., Jin C., Planavsky N. J., Algeo T. J., Cheng M., Yang X., Zhao Y. and Xie S. (2017) Coupled oceanic oxygenation and metazoan diversification during the early–middle Cambrian? *Geology* **45**, 743–746.
- Li D., Ling H., Shields-Zhou G. A., Chen X., Cremonese L., Och L., Thirlwall M. and Manning C. J. (2013) Carbon and strontium isotope evolution of seawater across the Ediacaran–Cambrian transition: Evidence from the Xiaotan section, NE Yunnan, South China. *Precambrian Res.* **225**, 128–147.
- Li G., Steiner M., Zhu X., Yang A., Wang H. and Erdtmann B. D. (2007) Early Cambrian metazoan fossil record of South China: Generic diversity and radiation patterns. *Palaeogeogr., Palaeoclimatol. Palaeoecol.* **254**, 229–249.
- Li Z., Bogdanova S. V., Collins A. S., Davidson A., Waele B. D., Ernst R. E., Fitzsimons I. C. W., Fuck R. A., Gladkochub D. P. and Jacobs J. (2008) Assembly, configuration, and break-up history of Rodinia: A synthesis. *Precambrian Res.* **160**, 179–210.
- Lu L. and Ji Y. (2013) Sequence stratigraphic framework and palaeogeography evolution of the Cambrian in Lower Yangtze area. *J. Palaeogeogr.* **15**, 765–776.
- Maloof A. C., Ramezani J., Bowring S. A., Fike D. A., Porter S. M. and Mazouad M. (2010) Constraints on early Cambrian carbon cycling from the duration of the Nemakit–Daldynian–Tommotian boundary ^{13}C shift, Morocco. *Geology* **38**, 623–626.
- Mei M., Ma Y., Zhang H. and Meng X. (2007) Sequence-stratigraphic frameworks for the Cambrian of the Upper–Yangtze region: ponder on the sequence stratigraphic background of the Cambrian biological diversity events. *J. Stratigraphy* **31**, 68–78.
- Möbius J. (2013) Isotope fractionation during nitrogen remineralization (ammonification): Implications for nitrogen isotope biogeochemistry. *Geochim. Cosmochim. Acta* **105**, 422–432.
- Montañez I. P., Osleger D. A., Banner J. L., Mack L. E. and Musgrove M. (2000) Evolution of the Sr and C isotope composition of Cambrian Oceans. *GSA Today* **10**, 1–7.
- Montoya J., Carpenter E. and Capone D. (2002) Nitrogen fixation and nitrogen isotope abundance in zooplankton of the oligotrophic North Atlantic. *Limnol. Oceanogr.* **47**, 1617–1628.
- Montoya J. P., Holl C. M., Zehr J. P., Andrew H., Villareal T. A. and Capone D. G. (2004) High rates of N_2 fixation by unicellular diazotrophs in the oligotrophic Pacific Ocean. *Nature* **430**, 1027–1032.
- Moore C. M., Mills M. M., Arrigo K. R., Berman-Frank I., Bopp L., Boyd P. W., Galbraith E. D., Geider R. J., Guieu C., Jaccard S. L., Jickells T. D., La Roche J., Lenton T. M., Mahowald N. M., Marañón E., Marinov I., Moore J. K., Nakatsuka T., Oschlies A., Saito M. A., Thingstad T. F., Tsuda A. and Ulloa O. (2013) Processes and patterns of oceanic nutrient limitation. *Nat. Geosci.* **6**, 701.
- Morris S. C. (2000) The Cambrian “explosion”: Slow-fuse or megatonnage? *Proc. Natl. Acad. Sci.* **97**, 4426–4429.
- Müller P. J. (1977) CN ratios in Pacific deep-sea sediments: Effect of inorganic ammonium and organic nitrogen compounds sorbed by clays. *Geochim. Cosmochim. Acta* **41**, 765–776.
- Nielsen A. T. and Schovsbo N. H. (2015) The regressive Early–Mid Cambrian ‘Hawke Bay Event’ in Baltoscandia: Epeirogenic uplift in concert with eustasy. *Earth-Sci. Rev.* **151**, 288–350.
- Peng S., Babcock L. and Cooper R. A. (2012) The Cambrian Period. *Geologic Time Scale*, 437–488.
- Prokopenko M. G., Hammond D. E., Berelson W. M., Bernhard J. M., Stott L. and Douglas R. (2006) Nitrogen cycling in the sediments of Santa Barbara basin and Eastern Subtropical North Pacific: Nitrogen isotopes, diagenesis and possible chemosymbiosis between two lithotrophs (Thioploca and Anammox)—“riding on a glider”. *Earth Planet. Sci. Lett.* **242**, 186–204.
- Robinson R. S., Kienast M., Albuquerque A. L., Altabet M., Contreras S., Holz R. D. P., Dubois N., Francois R., Galbraith E. and Hsu T. C. (2012) A review of nitrogen isotopic alteration in marine sediments. *Paleoceanography* **27**, 89–108.

- Schimmelmann A., Mastalerz M., Gao L., Sauer P. E. and Topalov K. (2009) Dike intrusions into bituminous coal, Illinois Basin: H, C, N, O isotopic responses to rapid and brief heating. *Geochim. Cosmochim. Acta* **73**, 6264–6281.
- Shu D., Isozaki Y., Zhang X., Han J. and Maruyama S. (2014) Birth and early evolution of metazoans. *Gondwana Res.* **25**, 884–895.
- Sigman D. M., Karsh K. L. and Casciotti K. L. (2009) Nitrogen isotopes in the ocean. *Encyclopedia Ocean Sci.*, 40–54.
- Sperling E. A. and Stockey R. G. (2018) The temporal and environmental context of early animal evolution: considering all the ingredients of an ‘explosion’. *Integr. Comp. Biol.* **58**, 605–622.
- Sperling E. A., Wolock C. J., Morgan A. S., Gill B. C., Kunzmann M., Halverson G. P., Macdonald F. A., Knoll A. H. and Johnston D. T. (2015) Statistical analysis of iron geochemical data suggests limited late Proterozoic oxygenation. *Nature* **523**, 451.
- Stüeken E. E. (2013) A test of the nitrogen-limitation hypothesis for retarded eukaryote radiation: Nitrogen isotopes across a Mesoproterozoic basal profile. *Geochim. Cosmochim. Acta* **120**, 121–139.
- Stüeken E. E., Kipp M. A., Koehler M. C. and Buick R. (2016) The evolution of Earth’s biogeochemical nitrogen cycle. *Earth-Sci. Rev.* **160**, 220–239.
- Stüeken E. E., Zaloumis J., Meixnerová J. and Buick R. (2017) Differential metamorphic effects on nitrogen isotopes in kerogen extracts and bulk rocks. *Geochim. Cosmochim. Acta* **217**, 80–94.
- Tesdal J.-E., Galbraith E. and Kienast M. (2013) Nitrogen isotopes in bulk marine sediment: linking seafloor observations with subseafloor records. *Biogeosciences* **10**, 101–118.
- Thunell R. C., Sigman D. M., Muller-Karger F., Astor Y. and Varela R. (2004) *Nitrogen isotope Dynamics of the Cariaco Basin*. Venezuela. Global Biogeochem. Cycles, p. 18.
- Tyrrell T. (1999) The relative influences of nitrogen and phosphorus on oceanic primary production. *Nature* **400**, 525–531.
- Wang D., Ling H., Struck U., Zhu X., Zhu M., He T., Yang B., Gamper A. and Shields G. A. (2018a) Coupling of ocean redox and animal evolution during the Ediacaran-Cambrian transition. *Nat. Commun.* **9**, 2575.
- Wang D., Struck U., Ling H., Guo Q., Shields-Zhou G. A., Zhu M. and Yao S. (2015) Marine redox variations and nitrogen cycle of the early Cambrian southern margin of the Yangtze Platform, South China: Evidence from nitrogen and organic carbon isotopes. *Precambrian Res.* **267**, 209–226.
- Wang J. and Li Z. (2003) History of neoproterozoic rift basins in South China: implications for Rodinia break-up. *Precambrian Res.* **122**, 141–158.
- Wang W.-L., Moore J. K., Martiny A. C. and Primeau F. W. (2019) Convergent estimates of marine nitrogen fixation. *Nature* **566**, 205.
- Wang X., Hu W., Yao S., Chen Q. and Xie X. (2011) Carbon and strontium isotopes and global correlation of Cambrian Series 2–Series 3 carbonate rocks in the Keping area of the northwestern Tarim Basin, NW China. *Mar. Pet. Geol.* **28**, 992–1002.
- Wang X., Jiang G., Shi X., Peng Y. and Morales D. C. (2018b) Nitrogen isotope constraints on the early Ediacaran ocean redox structure. *Geochim. Cosmochim. Acta* **240**, 220–235.
- Wang X., Jiang G., Shi X. and Xiao S. (2016) Paired carbonate and organic carbon isotope variations of the Ediacaran Doushantuo Formation from an upper slope section at Siduping, South China. *Precambrian Res.* **273**, 53–66.
- Wang X., Shi X., Jiang G. and Tang D. (2014) Organic carbon isotope gradient and ocean stratification across the late Ediacaran-Early Cambrian Yangtze Platform. *Sci. China Earth Sci.* **57**, 919–929.
- Xiang L., Schoepfer S. D., Shen S., Cao C. and Zhang H. (2017) Evolution of oceanic molybdenum and uranium reservoir size around the Ediacaran-Cambrian transition: Evidence from western Zhejiang, South China. *Earth Planet. Sci. Lett.* **464**, 84–94.
- Yang A., Zhu M. and Zhang J. (2005) Stratigraphic distribution and palaeogeographic control on the Early Cambrian Eodiscoids in Yangtze Platform. *J. Palaeogeogr.* **7**, 219–232.
- Yang A., Zhu M. and Zhang J. (2008) Chronostratigraphy of Cambrian Huangboling and Hetang formations in southern Anhui and western Zhejiang. *J. Stratigraphy* **32**, 343–352.
- Zhang Q. and Zhou Z. (1985) Early Cambrian trilobite fauna of Kunshan, Jiangsu. *Acta Palaeontologica Sinica* **24**, 259–266.
- Zhang X., Ahlberg P., Babcock L. E., Choi D. K., Geyer G., Gozalo R., Hollingsworth J. S., Li G., Naimark E. B. and Pegel T. (2017) Challenges in defining the base of Cambrian Series 2 and Stage 3. *Earth-Sci. Rev.* **172**, 124–139.
- Zhang X. and Shu D. (2014) Causes and consequences of the Cambrian explosion. *Sci. China Earth Sci.* **57**, 930–942.
- Zhang X., Sigman D. M., Morel F. M. M. and Kraepiel A. M. L. (2014) Nitrogen isotope fractionation by alternative nitrigenases and past ocean anoxia. *Proc. Natl. Acad. Sci.* **111**, 4782.
- Zhao Y., Babcock L. E., Peng J., Guo Q. and Wang Y. (2007) New data on the Wuliu-Zengjiayan section (Balang, South China), GSSP candidate for the base of Cambrian Series 3. *Memoir Assoc. Australasian Palaeontologists*, 57–65.
- Zhu M., Yang A., Yuan J., Li G., Zhang J., Zhao F., Ahn S. Y. and Miao L. (2018) Cambrian integrative stratigraphy and timescale of China. *Sci. China Earth Sci.* **61**.
- Zhu M., Zhang J., Li G. and Yang A. (2004) Evolution of C isotopes in the Cambrian of China: implications for Cambrian subdivision and trilobite mass extinctions. *Geobios* **37**, 287–310.
- Zhu M., Babcock L. E. and Peng S. (2006) Advances in Cambrian stratigraphy and paleontology: Integrating correlation techniques, paleobiology, taphonomy and paleoenvironmental reconstruction. *Palaeoworld* **15**, 217–222.
- Zhu X., Peng S. and Qi D. (2005) Early Cambrian trilobite fauna from Dongzhi, southern Anhui. *Acta Palaeontologica Sinica* **44**, 556–566.
- Zhuravlev A. Y. and Wood R. A. (1996) Anoxia as the cause of the mid–Early Cambrian (Botomian) extinction event. *Geology* **24**, 311.
- Zuo J., Peng S. and Zhu X. (2008) Carbon isotope composition of Cambrian carbonate rocks in Yangtze Platform, South China and its geological implications. *Geochimica* **37**, 118–128.